Original Research

Integrated Analysis of Single-cell and Bulk-RNA Sequencing Data to Identify Redox-related Genes as Prognostic Biomarkers and Therapeutic Targets of Lung Adenocarcinoma With Osimertinib Resistance

Chen Fang[1,2,3], Chaoxing Liu[1,2,3], Rong Qi[1,2,3], Jiabin Ding[1,2,3], Ting Luo[1,2,3], Feng Yu[1,3], Guohua Zhang[2,3], Chao Shi[1,2,3], Daya Luo[4], Feng Qiu[1,2,3,*]

[1]Department of Medical Oncology, The First Affiliated Hospital of Nanchang University, 330000 Nanchang, Jiangxi, China

[2]Nanchang Key Laboratory of Tumor Gene Diagnosis and Innovative Treatment Research, Gaoxin Branch of the First Affiliated Hospital of Nanchang University, 330000 Nanchang, Jiangxi, China

[3]Department of Oncology, Gaoxin Branch of the First Affiliated Hospital of Nanchang University, 330000 Nanchang, Jiangxi, China

[4]Department of Biochemistry and Molecular Biology, School of Basic Medical Sciences, Nanchang University, 330006 Nanchang, Jiangxi, China

*Correspondence: ndyfy01149@ncu.edu.cn (Feng Qiu)

Academic Editor: Eun Sook Hwang

Submitted: 8 May 2025   Revised: 21 August 2025   Accepted: 27 August 2025   Published: 25 September 2025

Abstract

Background: Acquired resistance limits the therapeutic efficacy of osimertinib in lung adenocarcinoma (LUAD). Redox homeostasis is crucial for LUAD progression. However, how redox imbalance interacts with the tumor microenvironment (TME) to drive osimertinib resistance (OR) remains unclear. **Methods**: The single-cell RNA sequencing (scRNA-seq) data GSE243562 were combined with the Cancer Genome Atlas (TCGA)-LUAD transcriptomes to map the TME cell population heterogeneity in osimertinib-resistant LUAD. Through univariate Cox regression and least absolute shrinkage and selection operator (LASSO) regularization, a prognostic signature founded on redox-related genes (RRGs) was built. Therapeutic compounds targeting these signature genes were prioritized by molecular docking. Their expression patterns were subsequently validated *in vitro*. **Results**: Cancer-associated fibroblasts (CAFs) were central hubs in the TME of osimertinib-resistant LUAD, exhibiting enhanced intercellular communication. Computational profiling identified 10 differentially expressed RRGs, predominantly enriched in CAFs. Using a six-gene signature comprising *AGER*, *CYP2J2*, *FMO2*, *HSPA1B*, *SOD3*, and *VASN*, we categorized LUAD patients into separate risk categories. High-risk patients showed significantly reduced survival, an immunosuppressive status, and a higher tumor mutation burden ($p < 0.05$). The overexpression of these six genes was confirmed in OR cells. Critically, inhibiting SOD3 restored osimertinib sensitivity *in vitro* ($p < 0.05$). Clinically, SOD3 expression was lower in patients sensitive to third-generation epidermal growth factor receptor-tyrosine kinase inhibitors (EGFR-TKIs) than in those with resistant disease. **Conclusions**: Targeting CAFs represents a promising strategy to overcome osimertinib resistance. Our six-gene redox signature offers a clinical framework for patient risk stratification and novel therapeutic strategy design. Future work will explore these targets to develop new treatments for LUAD.

Keywords: single-cell analysis; transcriptome; lung adenocarcinoma; osimertinib; oxidative stress; biomarkers

1. Introduction

Lung cancer is the leading cause of cancer-related deaths worldwide. Lung adenocarcinoma (LUAD) accounts for approximately 50% of all cases [1]. Epidermal growth factor receptor (EGFR)-mutant non-small cell lung cancer (NSCLC) patients respond significantly to EGFR-tyrosine kinase inhibitors (TKIs). This illustrates a major success for precision medicine [2]. Despite initial efficacy, acquired resistance to EGFR-TKIs ultimately drives disease progression, even with sequential first- to third-generation regimens [3]. Well-established resistance mechanisms to all three generations of EGFR-TKIs include secondary EGFR mutations, cellular-mesenchymal epithelial transition factor (c-MET) amplification, and lineage transformation [4]. In contrast, the mechanisms underlying clin-

ical drug tolerance remain elusive. Accumulating evidence supports the superior efficacy of combination targeted therapies for achieving more durable clinical responses [5]. Therefore, deciphering the molecular mechanisms of acquired resistance and identifying predictive biomarkers are imperative to optimizing therapeutic strategies and improving survival outcomes in NSCLC.

Cellular redox homeostasis is maintained by regulating the production of reactive oxygen species (ROS) and the activity of antioxidant defense systems [6]. Disrupted redox homeostasis is a cancer hallmark, regulated by conserved redox-related genes (RRGs) [7,8]. Unlike normal cells, cancers exhibit a dysregulated redox state with concurrent ROS elevation and enhanced antioxidant defense, with a consequence of metabolic reprogramming, genomic

instability, mitochondrial dysfunction, and tumor microenvironment (TME) adaptations [9,10]. ROS play dual and context-dependent roles in carcinogenesis. In NSCLC, this redox interplay influences progression, drug resistance, and apoptosis. Here, differentially expressed RRGs are key regulators, particularly of resistance mechanisms, making them promising therapeutic targets to overcome NSCLC resistance, metastasis, and recurrence [11–13]. However, the prognostic role and functional mechanisms of RRGs in NSCLC lack clarity.

Single-cell RNA sequencing (scRNA-seq) deciphers tissue heterogeneity by categorizing cells, advancing precision medicine [14]. Beyond defining cell types, it precisely defines gene function within heterogeneous populations to reveal cancer-promoting pathways [15]. Leveraging these advantages, studies increasingly identify novel biomarkers by integrating scRNA-seq with bulk transcriptome data [16,17]. Given the complex landscape of therapy resistance, we combined these approaches to develop a prognostic signature for improving NSCLC outcome prediction and guiding therapy.

Using single-cell resolution mapping, we identified differentially expressed redox-related genes (DE-RRGs) in malignant cell clusters of osimertinib-resistant LUAD. Integration with bulk transcriptomics established a six-gene prognostic signature (*AGER*, *CYP2J2*, *FMO2*, *HSPA1B*, *SOD3*, *VASN*). Immune profiling and molecular docking revealed the signature's therapeutic potential, which was confirmed by the upregulated DE-RRG expression we observed in resistant cells. Crucially, SOD3 knockdown restored osimertinib sensitivity *in vitro*, and lower SOD3 levels were clinically associated with sensitivity to third-generation EGFR-TKIs. Our work defines clinically actionable biomarkers and reveals novel therapeutic vulnerabilities in treatment-resistant LUAD.

2. Material and Methods

2.1 Bioinformatic Data Curation

The scRNA-seq data GSE243562 were obtained from the gene expression omnibus (GEO) database (https://www.ncbi.nlm.nih.gov/geo/), using patient-derived xenograft (PDX) models of osimertinib-treated lung cancer. Samples GSM7790998 and GSM77901000 were classified as osimertinib sensitivity (OS), while GSM7790999 and GSM77901001 were classified as osimertinib resistance (OR). Bulk RNA-seq data were further acquired from the cancer genome atlas (TCGA)-LUAD cohort (https://portal.gdc.cancer.gov) and the GSE72094 dataset. Model development was conducted in the TCGA-LUAD cohort, with independent validation performed using the GSE72094 dataset. All datasets were standardized using R software (v4.3.0, https://cran.r-project.org/bin/windows/base/old/4.3.0/R-4.3.0-win.exe).

2.2 Quality Control of Single-cell Datasets and Cell Type Annotation

Quality control was performed using the "Seurat" package (v5, https://github.com/satijalab/seurat). Cells were filtered based on the following criteria: nCount_RNA (1000–50,000), nFeature_RNA (200–10,000), percentage of mitochondrial genes (<15%), and percentage of red blood cell genes (<5%). Data were normalized using the "SCTransform" method. Dimensionality reduction was conducted using 12 principal components, and cells were clustered at a resolution of 1.0. Cell populations were visualized using *t*-distributed stochastic neighbor embedding (*t*-SNE). The top 20 differentially expressed genes (DEGs) per cluster were analyzed. Cell types were annotated by integrating evidence from the literature, the CellMarker 2.0 database (http://117.50.127.228/CellMarker/index.html), and the "SingleR" package (v2.10.0, https://bioconductor.org/packages/SingleR).

2.3 RRG Scoring

The 940 RRGs were sourced from MsigDB (https://www.gsea-msigdb.org/gsea/msigdb) and published literature [18] (**Supplementary Table 1**). Marker genes were selected based on significant population specificity (adj_p < 0.05 and avg_log 2FoldChange >1.5) between the OR- and OS-groups. The intersecting genes between these markers and the RRG set were identified as DE-RRGs using a Venn diagram. For the OR group, cellular activity scores were calculated for these DE-RRGs using the "AUCell" package (v1.16.0, https://github.com/aertslab/AUCell). The AUCell_exploreThresholds function was then applied to define the threshold for identifying cells with active RRGs trait. Finally, these cells were visualized on a *t*-SNE plot, color-coded by their respective clusters.

2.4 Pseudotime Analysis and Cell-cell Communication

Pseudotime analysis was performed using the "Monocle" package (v2.26.0, http://cole-trapnell-lab.github.io/monocle-release). The fibroblast cluster was isolated and subsequently classified into subpopulations based on established cell marker genes. The "DDRTree" method was then applied for dimensionality reduction, and cell differentiation states were ordered using the "orderCells" function. Expression patterns of the DE-RRGs were mapped along the inferred pseudotime. The intercellular communication was analyzed with the "CellChat" package (v2.1.0, https://github.com/jinworks/CellChat) to quantify and visualize receptor-ligand interactions.

2.5 Establishment and Assessment of the Prognostic Risk Model

The DEGs of TCGA-LUAD cohort was analyzed using DESeq2 (|logFC| ≥1, adjusted p < 0.05). The resulting DEGs were visualized with waterfall plots and heatmaps. Survival-associated DE-RRGs were initially

identified through univariate Cox regression analysis. Subsequently, significant genes were selected using least absolute shrinkage and selection operator (LASSO) regression, and a prognostic model was constructed via multivariate Cox regression. This model was validated in the independent GSE72094 cohort. To evaluate clinical utility, receiver operating characteristic (ROC) curves were plotted and a nomogram was constructed. For comparative analysis, three established LUAD prognostic signatures were curated from the literature [19–21] (**Supplementary Table 2**). Finally, risk scores were calculated by matrix multiplication of scaled expression values and regression coefficients, and model performance was compared using the C-index and area under curve (AUC).

2.6 Functional Enrichment Analysis

Gene Ontology (GO, http://geneontology.org/) and Kyoto Encyclopedia of Genes and Genomes (KEGG, https://www.kegg.jp) pathway analyses were performed to characterize the functions and pathways associated with DEGs. Enrichment analyses for biological processes, molecular functions, cellular components, and KEGG pathways were conducted using the "clusterProfiler" package (v4.16.0, https://bioconductor.org/packages/clusterProfiler), with a statistical significance cutoff of $p < 0.05$.

2.7 Immune Cell Infiltration

The association between the prognostic risk signature and immune infiltration was assessed by single-sample gene set enrichment analysis (ssGSEA) to quantify immune cell abundance in the TCGA-LUAD cohort. Additionally, a Pearson correlation analysis was performed between the six DE-RRGs and the infiltrating immune cells.

2.8 Gene Mutation Analysis

Somatic mutation analysis was performed on TCGA datasets using the "maftools" package (v2.24.0, https://bioconductor.org/packages/maftools). Differences in tumor mutational burden (TMB) across risk groups were then assessed using the Tumor Immune Dysfunction and Exclusion (TIDE) platform (http://tide.dfci.harvard.edu/), integrated with copy number variation data.

2.9 Drug Screening and Docking

Autodock (Linux, v4.2, Olson, CA, USA) was employed to perform molecular docking analyses of small molecule compounds that interact with prognostic genes. Initially, the comparative toxicogenomics database (CTD, https://ctdbase.org/) was queried to extract bioactive compounds corresponding to prognostic genes and subsequently their structural information were obtained from the PubChem database (https://pubchem.ncbi.nlm.nih.gov/). Then, we accessed and downloaded the biological macromolecular structures corresponding to the prognostic genes from the UniProt database (https://www.uniprot.org/). Standardized docking of macromolecule-ligand complexes identified strongest binders via energy minimization. Structural representations were rendered in PyMol v2.6 (DeLano Scientific LLC, Palo Alto, CA, USA).

2.10 Cell Culture

NSCLC cell lines HCC827 (EGFR exon 19 deletion) and H1975 (EGFR L858R and T790M mutations) (authenticated via STR profiling) were sourced from the Type Culture Collection of the Chinese Academy of Sciences (Shanghai, China). Osimertinib-resistant derivatives (HCC827/OR, H1975/OR) were established through stepwise exposure to osimertinib (10 nM → 5 μM), selecting clones proliferating at 5 μM. All lines were cultured in RPMI-1640 supplemented with 10% FBS and penicillin/streptomycin at 37 °C/5% CO_2, with routine mycoplasma screening pre-experimentation. All cell lines were tested negative for mycoplasma.

2.11 Reverse Transcription Quantitative Polymerase Chain Reaction (RT-qPCR)

Total RNA was extracted from cells using TRIzol (15596018CN, Invitrogen, Carlsbad, CA, USA). Subsequently, 1 μg of the total RNA was converted into cDNA with the help of the PrimeScript RT Reagent Kit (AE311-02, TransGen Biotech, Beijing, China). For qPCR, the SYBR Green PCR Master Mix in the kit above was utilized, and the results were analyzed using GraphPad Prism (v7.0.4, GraphPad Software, San Diego, CA, USA) based on One-way ANOVA. Human GAPDH (B661104-0001, Sangon Biotech (Shanghai) Co., Ltd., Shanghai, China) served as the internal housekeeping control. The sequences for PCR primers were provided in **Supplementary Table 3**.

2.12 Western Blotting

Total protein was extracted via a combination of radioimmunoprecipitation and lysis buffer. The isolated proteins underwent 10% sodium dodecyl sulfate polyacrylamide gel electrophoresis (SDS-PAGE), followed by transfer onto polyvinylidene fluoride membranes. These membranes were then blocked with a 5% milk solution and incubated overnight at 4 °C with the primary antibodies. Subsequently, the membranes were treated with horseradish peroxidase-conjugated secondary antibodies (1:1000, SA00001-2, Proteintech, Wuhan, Hubei, China) relevant to the primary ones used. Signal detection was carried out with an enhanced chemiluminescence detection kit (New Cell & Molecular Biotech, P10100, Suzhou, Jiangsu, China). The primary antibodies employed included SOD3 (1:1000, HA721408, HuaBio, Hangzhou, Zhejiang, China) and GAPDH (1:15000, 10494-1-AP, Proteintech, Wuhan, Hubei, China).
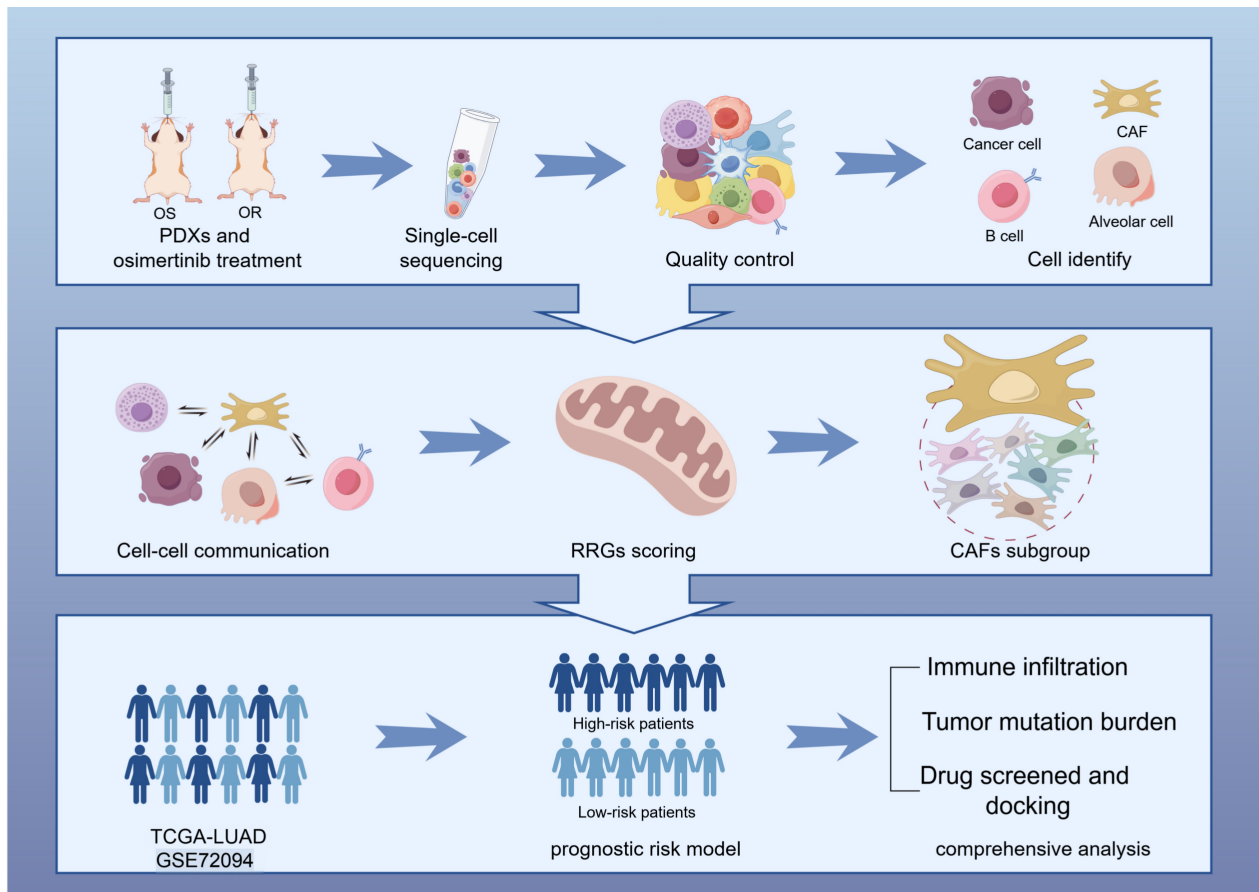
Fig. 1. Research pipeline. OS, osimertinib sensitivity; OR, osimertinib resistance; PDX, patient-derived xenograft; CAFs, cancer-associated fibroblasts; RRGs, redox-related genes; LUAD, lung adenocarcinoma; TCGA, the cancer genome atlas. The Figure was created with Figdraw.

2.13 ShRNA Transfections

Lentiviral shRNA vectors against SOD3 (shSOD3) and non-targeting controls (shNC) were custom-synthesized by Genepharma (Shanghai, China) with sequence verification. Transfection was performed using jetPRIME® transfection reagent (No: 114–115, Polyplus-transfection®, Strasbourg, Alsace, France) at 1:2 DNA: reagent ratio. Cells at 70–80% confluency in 6-well plates were transfected with 2 µg shRNA vectors per well following manufacturer protocol. The specific sequence is as follows: shSOD3: 5′-GGAGTGGATCCGAGACATGTA-3′; shNC: 5′-CGGGCGACTTCGGCAACTT-3′.

2.14 CCK8 Assay

Cell proliferation was quantified using Cell Counting Kit-8 (CCK-8; No. K1018, APExBIO, Houston, TX, USA) according to manufacturer specifications. Cells (2×10^3/well) were plated in 96-well format, pre-incubated 24 h (37 °C/5% CO_2), and exposed to osimertinib (0, 0.016, 0.08, 0.4, 2, 10 µM; MedChemExpress HY-15772) for 72 h. CCK-8 reagent (10 µL/well) was added followed by 2 h incubation at 37 °C. The absorbance was recorded at a wavelength of 450 nm.

2.15 Measurement of ROS

ROS quantification used the Reactive Oxygen Species Assay Kit (S0033S, Beyotime, Shanghai, China). Cells stained with 10 µM DCFH-DA (serum-free medium, 37 °C, 30 min) were analyzed on a CytoFLEX LX flow cytometer (DxFLEX, Beckman Coulter, Inc., Brea, CA, USA) with FlowJo v10.9.0 (BD Biosciences, Franklin Lake, NJ, USA).

2.16 Patients and Specimens

Paraffin-embedded tissue samples from 24 pathologically confirmed EGFR-mutant NSCLC patients were included before targeted therapy. All cases received third-generation EGFR-TKIs targeted therapy (Osimertinib, n = 12; Almonertinib, n = 8; Furmonertinib, n = 4). The samples were derived from the pathological specimen bank of the First Affiliated Hospital of Nanchang University [Ethics Approval Number: (2024) CDYFYYLK (10-005)]. All patients or their guardians signed informed consent forms.

2.17 Immunohistochemistry (IHC)

Following preparation from surgical/biopsy specimens, 4-µm-thick Formalin-Fixed, Paraffin-Embedded tissue sections were processed through a 20-minute antigen

retrieval step in 95 °C citrate buffer (pH 6.0). Immunostaining was performed using human monoclonal anti-SOD3 antibody (1:200, HA721408, HuaBio, Hangzhou, Zhejiang, China) incubated overnight at 4 °C. Detection employed HRP-conjugated secondary antibody (G1302, Servicebio, Wuhan, Hubei, China) and DAB chromogen (P0203, Beyotime, Shanghai, China) as previously described [22].

2.18 Statistical Analysis

Statistical analyses utilized R Studio (v23.3.0, Posit Software, Boston, MA, USA). Normality-conforming continuous variables underwent independent t-tests for group comparisons, while non-parametric distributions employed Wilcoxon tests. Significance was defined at $p < 0.05$.

3. Results

3.1 Single-cell Atlas of LUAD Exhibiting Sensitivity and Resistance to Osimertinib

Fig. 1 outlines the study design. We analyzed four osimertinib-treated PDX samples by scRNA-seq. After rigorous quality control, we retained 12,327 high-quality cells for analysis, including 9874 from osimertinib-sensitive tumors and 2453 from resistant tumors. Subsequent t-SNE visualization of the dataset resolved 27 unique clusters, which we classified into 10 distinct cell types: epithelial cells, fibroblasts, Treg cells, alveolar cells, CD8+ T cells, cancer cells, dendritic cells, B cells, monocytes/macrophages, and mesenchymal cells (Fig. 2A,B). The t-SNE plot further revealed clear clustering by tumor origin (Fig. 2C). We validated these cellular subclasses with 10 established marker genes (Fig. 2D) and highlighted the top five DEGs per cluster in a heatmap (Fig. 2E). Analysis of cellular composition revealed variable cell-type proportions across samples (Fig. 2F). Alveolar cells constituted the largest population in three samples (GSM7790998, GSM7790999, GSM7791000), whereas epithelial cells predominated in the remaining sample (Fig. 2G). Notably, we observed significant differences in cellular composition between OS- and OR-LUAD tissues (Fig. 2H).

3.2 Cell–cell Communication Analysis

We mapped a global cell communication network across major cell types using single-cell data (Fig. 3A). Compared to OS-samples, OR-samples exhibited markedly stronger interactions between cancer-associated fibroblasts (CAFs) and other cell types, particularly epithelial and immune cells (Fig. 3B). Our systematic interrogation of ligand-receptor networks revealed OR-specific enrichment of PPIA-BSG signaling between tumor cells and Tregs, epithelial cells, and CAFs (**Supplementary Fig. 1A,B**). Fibroblast-focused analysis further showed intensified CAF-tumor crosstalk in OR samples, primarily mediated by WNT7B-(FZD2 + LRP5) and MDK-SDC1 pairs, which were significantly weaker in OS samples (Fig. 3C,D). We also observed reduced COL1A1-SDC1 and

COL1A1-SDC4 interactions in the OS group. Together, these results suggest that enhanced CAF-tumor communication contributes to osimertinib resistance.

3.3 Identification and Evaluation of DEGs Related to Redox Processes

We detected altered EGFR phosphorylation with concurrent increases in focal adhesion kinase (FAK) and protein kinase B (AKT) phosphorylation in OR cells, indicating potential EGFR-independent resistance mechanisms (**Supplementary Fig. 2A**). OR-related DEGs were primarily associated with ROS pathways (**Supplementary Fig. 2B–D**). By cross-referencing 149 OR-specific markers with 940 RRGs, we identified 10 DE-RRGs: *ABCA1*, *AGER*, *CYP2J2*, *FMO2*, *GSTA4*, *HSPA1B*, *JUN*, *KLF2*, *SOD3*, and *VASN* (Fig. 4A). Then, we analyzed relationships among the 10 DE-RRGs (Fig. 4B). Significant positive correlations (all $p < 0.001$) occurred between: *JUN* and *KLF2* (R = 0.28), *HSPA1B* (R = 0.45), *FMO2* (R = 0.15); *HSPA1B* and *KLF2* (R = 0.18); *AGER* and *VASN* (R = 0.17), SOD3 (R = 0.26), *FMO2* (R = 0.19); *SOD3* and *FMO2* (R = 0.18). Expression analysis across cell types in OR-group showed broad distribution of *AGER*, *JUN*, *GSTA4*, *HSPA1B*, and *SOD3*, while *VASN* and *KLF2* expression was enriched in fibroblasts (Fig. 4C), suggesting cellular cooperation promotes resistance. We scored individual cells for DE-RRG activity using AUCell, finding 1129 cells exceeding the significance threshold (AUC >0.13) (Fig. 4D). These high-activity cells were predominantly epithelial cells and fibroblasts (Fig. 4E). Functional enrichment analysis linked these DE-RRGs to oxygen radical response, mitochondrial outer membrane, ubiquitin ligase binding, and advanced glycation end products - receptor for advanced glycation end products (AGE-RAGE) signaling, apoptosis, and viral carcinogenesis pathways (Fig. 4F).

3.4 Analysis of the Clustering and Trajectory of CAF Subdivisions

We isolated 187 CAFs and classified them into six distinct subtypes based on specific marker expression: *KRT17* + mesCAFs, *BRAP* + Fib1, *SLC35A5* + Fib2, *PSMD9* + panCAFs, *RPS3AP26* + Fib3, and *CARD9* + iCAFs (Fig. 5A,B). Evaluation of the 10 DE-RRGs across these subtypes revealed ubiquitous expression of *JUN* and *HSPA1B* in all CAFs, while *CYP2J2* showed minimal expression in any subgroup (Fig. 5C). Using computational trajectory inference, we modeled CAF differentiation through seven distinct states (color-coded in Fig. 5D). Pseudotime analysis indicated that differentiation proceeds from right to left, with darker blue hues representing earlier stages (Fig. 5F). The panCAFs emerged primarily at early differentiation stages and demonstrated potential to evolve into mesothelial CAF (mesCAFs) and other CAF types (Fig. 5E). Expression dynamics of the 10 DE-RRGs varied significantly along this differentiation trajectory (Fig. 5G).
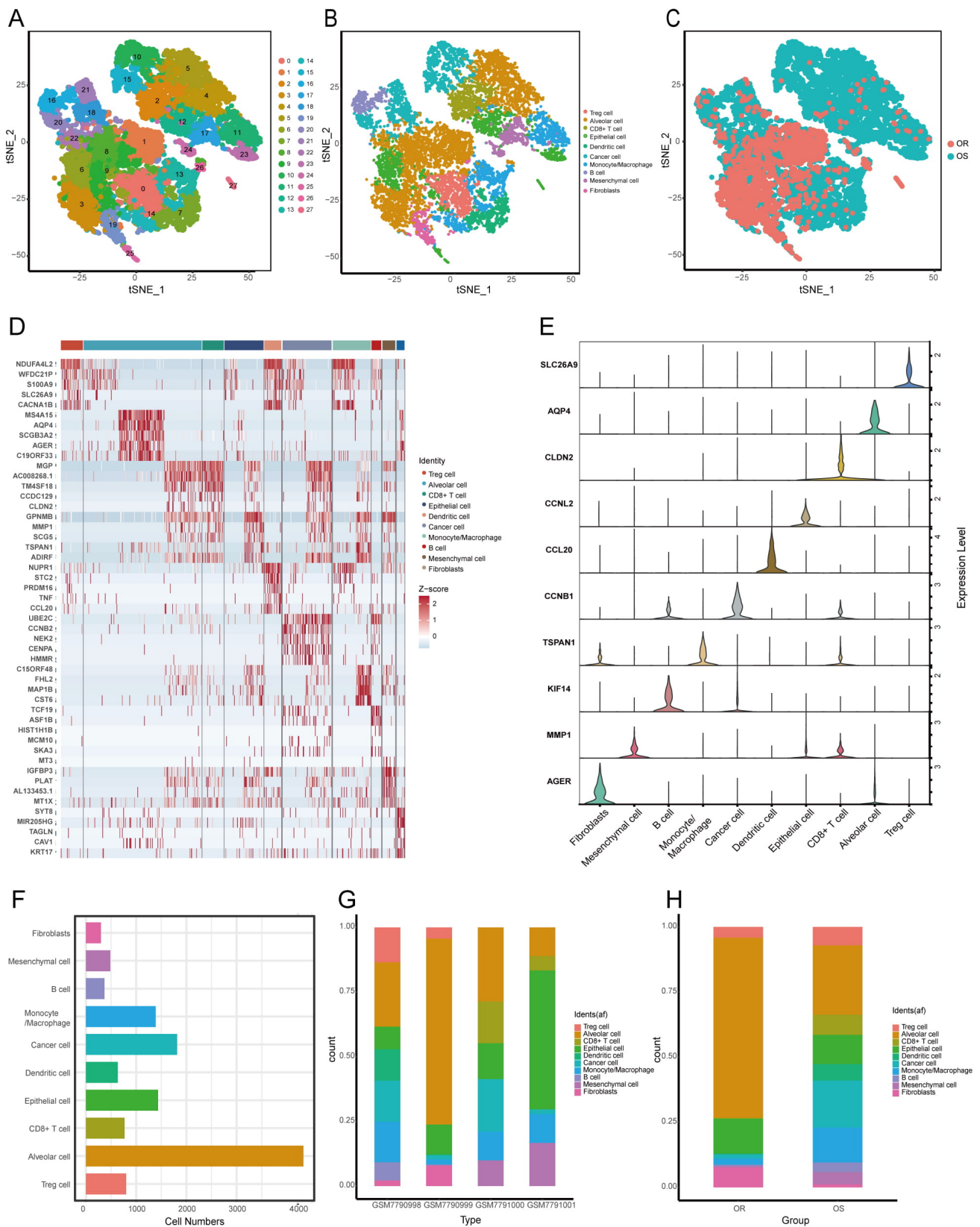
Fig. 2. Cell Populations in OS- and OR-LUAD tumor microenvironment (TME). (A) *t*-SNE projection of 27 distinct cell clusters. (B) *t*-SNE visualization color-coded by cell type. (C) *t*-SNE visualization color-coded by sample origin. (D) Heatmap illustrating differentially expressed marker genes (rows) across 10 distinct cell clusters. (E) Violin plots showing expression distribution of diagnostic marker genes per cell cluster. (F) The overall quantity of each cell type. (G) Cellular cluster distribution across four PDX samples. (H) Proportion of cell populations in the OS and OR sample groups. *t*-SNE, *t*-distributed stochastic neighbor embedding.
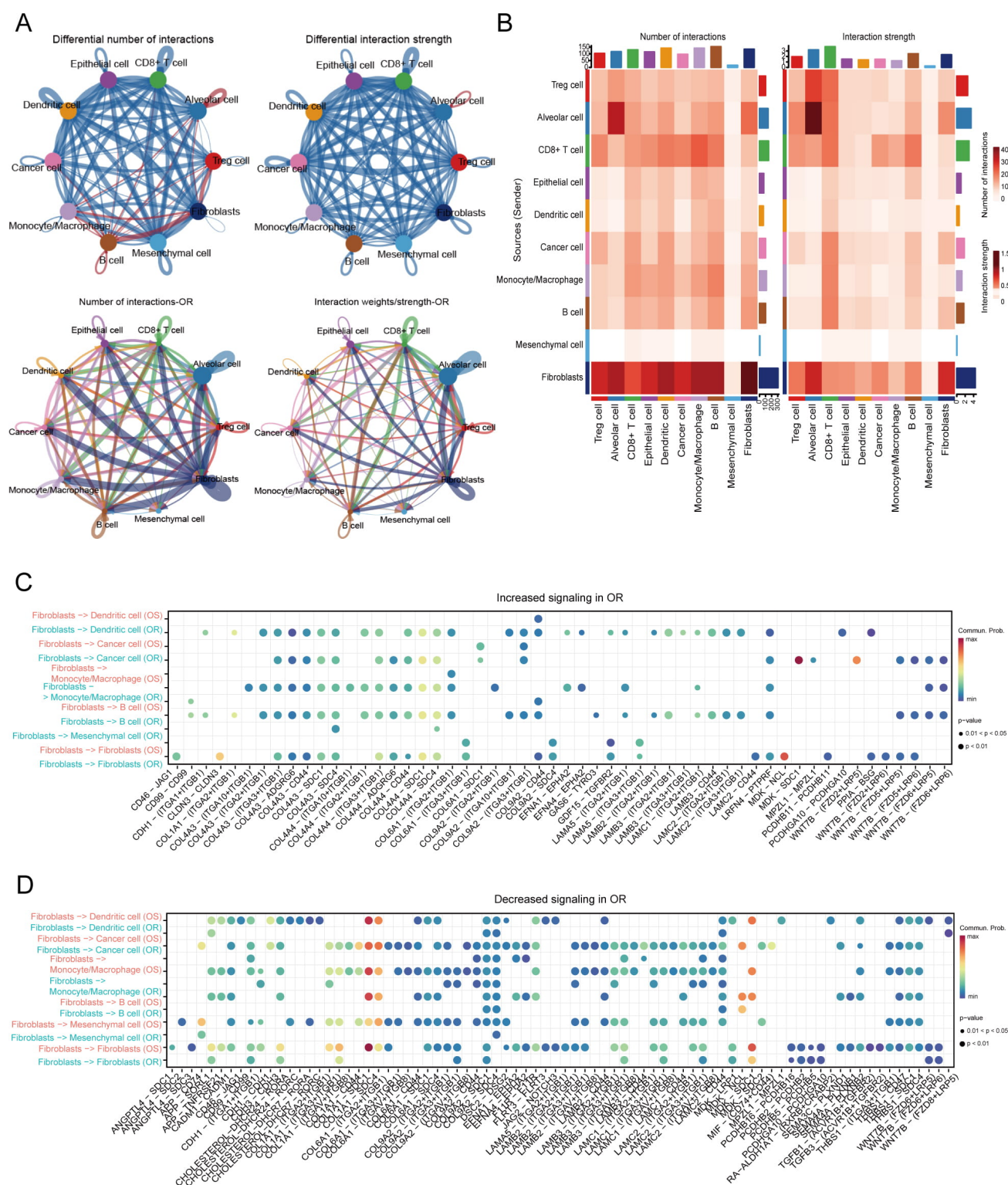
Fig. 3. Communication between cells within OR clusters. (A) Communication networks and interactions among different cell types in OS and OR samples; OS is shown in the top row, OR is shown in the bottom row. (B) Cell–cell communication is illustrated through the number of interactions (left) and the strength of those interactions (right). The blue blocks indicate down-regulated interactions, whereas the red blocks indicate up-regulated communication within the OR group. (C,D) Alterations in the interaction networks of receptor–ligand interactions between fibroblasts and various other cell types were observed in both the OS and OR groups. The Y-axis denotes the cell types, whereas the X-axis illustrates the receptor–ligand pairs.
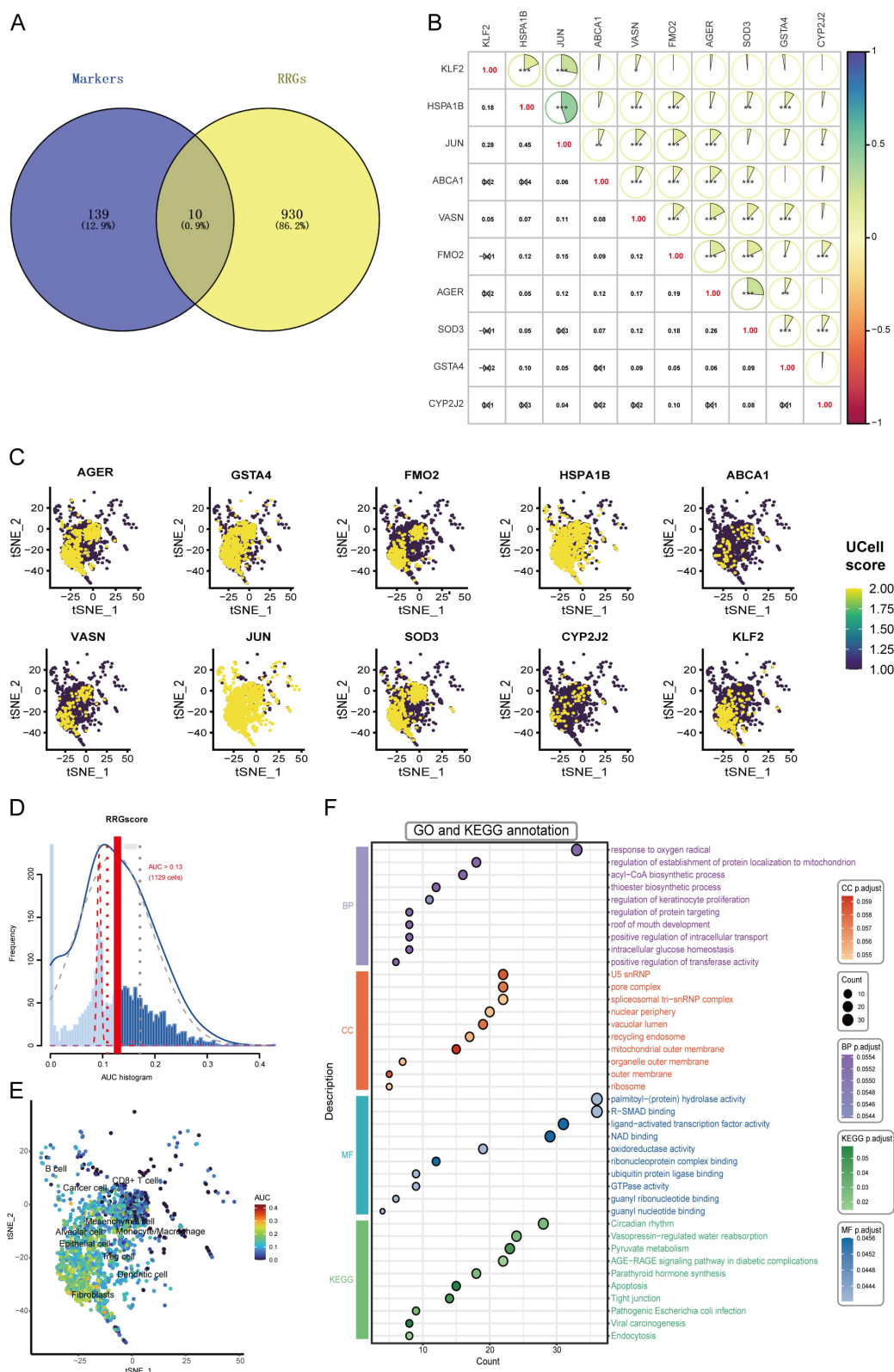
Fig. 4. Identification of DE-RRGs and scoring. (A) Venn diagram identifying DE-RRGs at the intersection of OR-specific markers and RRGs. (B) Correlation analysis of the 10 identified DE-RRGs, displaying pairwise correlation coefficients; $*p < 0.05$, $**p < 0.01$, $***p < 0.001$. (C) t-SNE plots visualizing spatial distribution of 10 DE-RRGs across OR cells. (D) AUC histogram of AUCell scores for 10 DE-RRGs. (E) t-SNE visualization of RRG activity scores across cell populations. (F) GO and KEGG pathway analyses of DEGs stratified by RRG scores. DE-RRGs, differentially expressed redox-related genes; GO, Gene Ontology; KEGG, Kyoto Encyclopedia of Genes and Genomes.
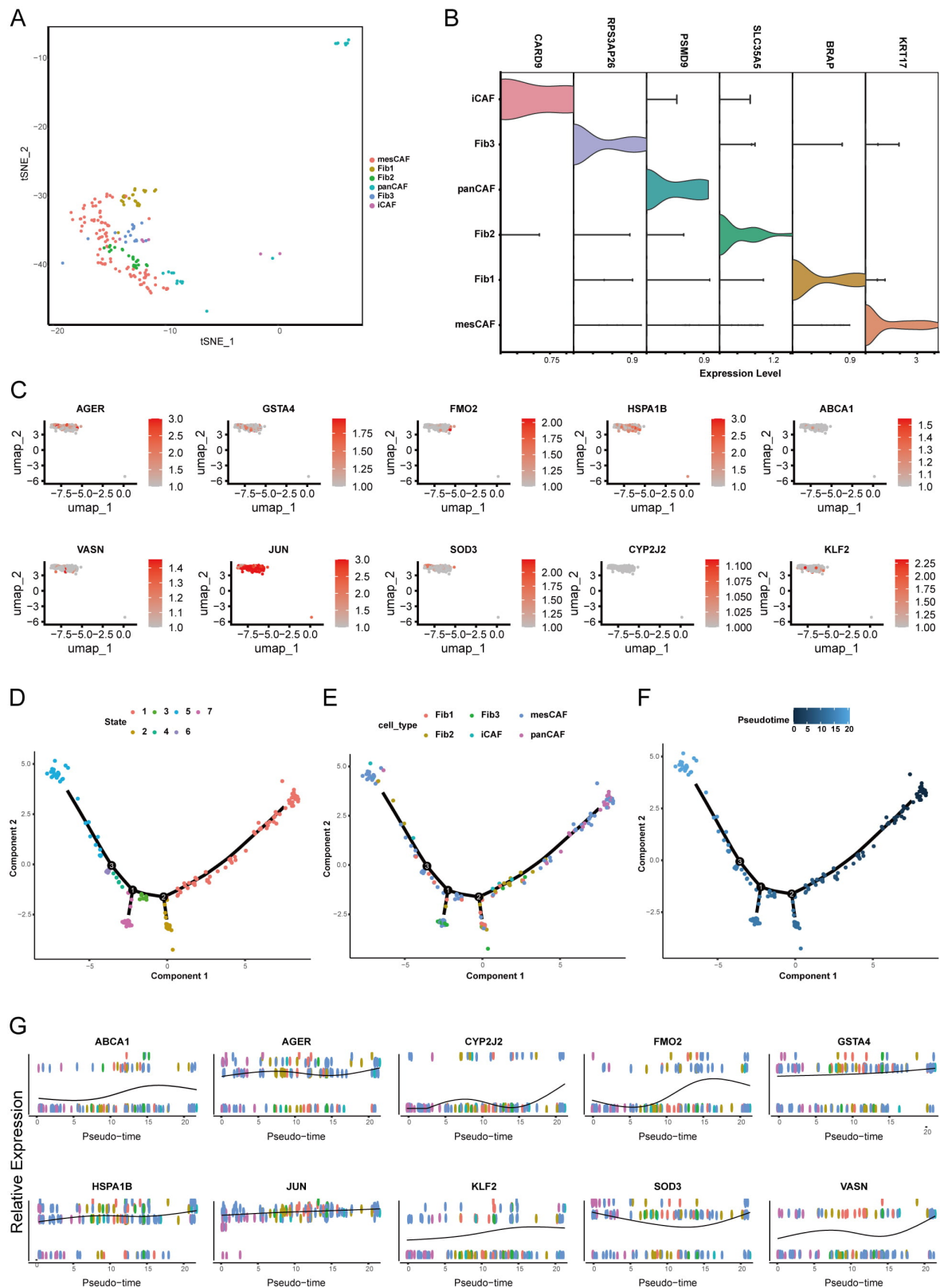
Fig. 5. Analysis of CAF subdivision and trajectory assessment. (A) *t*-SNE visualizations depicting 6 distinct subpopulations of fibroblasts in the OR group. (B) Violin plots illustrating the expression levels of cellular markers across 6 distinct CAF subpopulations. (C) UMAP plots of 10 DE-RRGs across 6 CAF subpopulations. (D–F) Differentiation trajectory of CAFs, represented by their state (D), cell type (E), and pseudotime (F). (G) The expression profiles of 10 DE-RRGs throughout the differentiation pseudotime trajectory. UMAP, Uniform Manifold Approximation and Projection.

Throughout the differentiation trajectory, DE-RRGs such as *CYP2J2*, *SOD3*, and *VASN* gradually increased. In contrast, *ABCA1*, *FMO2*, and *KLF2* displayed a decreasing trend. Additionally, *AGER*, *GSTA4*, *HSPA1B*, and *JUN* did not demonstrate any significant trend during the trajectory analysis.

3.5 Prognostic Risk Assessment Model Based on 10 DE-RRGs

We analyzed bulk transcriptome data from 513 TCGA-LUAD patients, identifying 21,494 DEGs between tumor and normal adjacent tissues (14,884 upregulated and 6610 downregulated) visualized in a waterfall plot (Fig. 6A). Among these, we identified 10 DE-RRGs shown in a heatmap (Fig. 6B). Using complete survival data from 513 cases (**Supplementary Table 4**), univariate Cox regression assessed the prognostic value of these DE-RRGs. Subsequent LASSO and multivariate Cox analyses refined the signature to six genes (*AGER*, *CYP2J2*, *FMO2*, *HSPA1B*, *SOD3*, *VASN*) and calculated their risk coefficients (**Supplementary Fig. 3A,B**). The resulting risk score formula was: risk score = $(-0.048 \times AGER) + (0.090 \times CYP2J2) + (-0.053 \times FMO2) + (0.112 \times HSPA1B) + (-0.052 \times SOD3) + (0.027 \times VASN)$. High-risk patients showed significantly worse overall survival ($p = 0.006$; Fig. 6C). The prognostic model demonstrated strong predictive power for 1-, 3-, and 5-year survival (AUC = 0.701, 0.753, and 0.687, respectively; Fig. 6D). We validated these findings in the GSE72094 cohort, where K–M curves confirmed significant survival stratification ($p < 0.001$, Fig. 6E) and ROC curves showed consistent predictive performance (1-year: 0.692; 3-year: 0.678; 5-year: 0.638; Fig. 6F). Comparative analysis showed our signature had superior predictive accuracy to existing LUAD signatures in the TCGA cohort (Fig. 6G). We developed a prognostic nomogram incorporating the risk score and key clinical variables (Fig. 6H) and derived cumulative risk points by summing weighted factor values. Calibration curves confirmed accurate 3-year survival prediction (Fig. 6I), while decision curve analysis demonstrated strong clinical utility across most threshold probabilities (Fig. 6J).

3.6 Assessment of Functional Enrichment Derived From the Risk Model

Survival differences between the two risk groups revealed significant genomic heterogeneity. To explore the underlying mechanisms, we performed GSEA analysis. High-risk patients showed activation of cell cycle, DNA replication, proteasome, ribosome, and spliceosome pathways, but suppression of asthma-related immunity, intestinal immune network, lupus erythematosus, and vascular smooth muscle contraction pathways (Fig. 7A,B). GO analysis confirmed that DEGs significantly affected tumor-promoting biological processes and cellular functions (Fig. 7C). KEGG analysis further confirmed the strong influence of these DEGs on key signaling pathways (Fig. 7D), ultimately explaining the prognostic differences observed in LUAD patients.

3.7 Assessment of the Immune Microenvironment and Gene Mutations

We next investigated the link between the risk signature and the tumor immune microenvironment. We observed an inverse correlation between risk score and immune clearance, but a positive correlation with immunosuppressive activity across multiple immune cell types. For example, CD8+ T cell levels were significantly higher in the low-risk group than in the high-risk group (Fig. 8A,B). Correlation analysis revealed distinct immune interaction patterns for the six prognostic RRGs (Fig. 8C). *AGER*, *FMO2*, *SOD3*, and *VASN* showed positive correlations with M2 macrophages and negative correlations with CD4+ T cell activation. Conversely, *CYP2J2* and *HSPA1B* expression correlated negatively with neutrophil and plasma cell infiltration. These results confirm that the six RRGs critically shape the immune landscape in LUAD. We also examined single nucleotide variations between risk groups. In high-risk patients, *TP53* (54%), *TTN* (53%), *CSMD3* (44%), *MUC16* (42%), and *RYR2* (40%) showed the highest mutation frequencies (Fig. 9A). The same five genes showed the highest mutation frequency in the low-risk group, albeit in a slightly different order (Fig. 9B). Thus, we combined *TP53* mutations and risk scores to predict LUAD patient prognosis. Regardless of *TP53* status, high-risk patients exhibited markedly reduced survival (Fig. 9C). TMB positively correlated with risk score (Fig. 9D, **Supplementary Fig. 4A**). Moreover, our signature achieved higher AUC values than TMB in the TCGA cohort (**Supplementary Fig. 4B**). Finally, the high-risk group exhibited higher GISTIC scores and more frequent amplification and deletion events than the low-risk group (Fig. 9E).

3.8 Docking of Small-molecule Compounds Related to Prognostic Genes

Our molecular docking analysis identified six small-molecule inhibitors targeting prognostic RRGs. Rotenone effectively bound AGER (–6.4 kcal/mol) and decreased its mRNA expression (Fig. 10A). MRK003 showed strong binding to CYP2J2 (–10.1 kcal/mol; Fig. 10B), while lutein effectively targeted FMO2 (–9.5 kcal/mol; Fig. 10C). Methotrexate (MTX) emerged as a potent binder of HSPA1B (–10.8 kcal/mol; Fig. 10D). Epigallocatechin gallate (EGCG) bound SOD3 with high affinity (–7.4 kcal/mol; Fig. 10E), reduced its protein levels (**Supplementary Fig. 5A,B**), and exhibited an IC50 of 25.91 µM in HCC827/OR cells. Sunitinib efficiently targeted VASN (–8.2 kcal/mol) and suppressed its expression (Fig. 10F). Together, these compounds provide a targeted therapeutic strategy against osimertinib-resistant NSCLC.
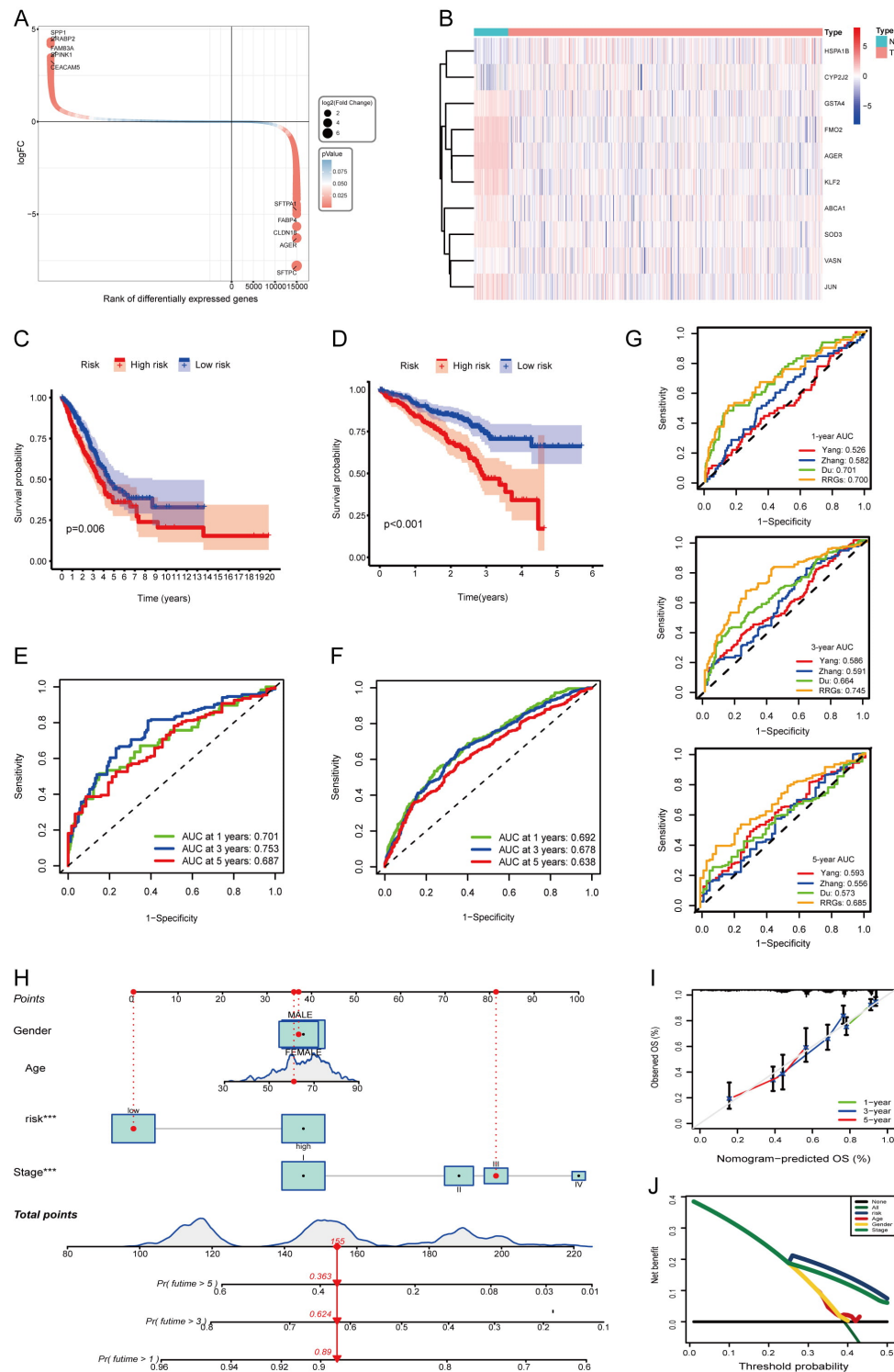
Fig. 6. Construction and validation of the prognostic risk model. (A) Evaluation of the DEGs between the normal and tumor groups. Each gene is represented by a circle, with its color indicating the level of significance regarding the differences in expression. (B) Heatmap illustrating the expression of 10 DE-RRGs between normal and tumor samples derived from the TCGA-LUAD cohort. (C,D) K–M curves illustrating the survival outcomes of patients categorized into two risk groups within the TCGA-LUAD cohort (C) and GSE72094 cohort (D). (E,F) The ROC curves were constructed to evaluate the survival rates at 1-year, 3-year, and 5-year intervals for the TCGA-LUAD cohort (E) and GSE72094 cohort (F). (G) Comparison of time-dependent area under the ROC curve among prognostic signatures at 1-, 3-, and 5-years in the TCGA-LUAD dataset. (H) The specifics of the nomogram are provided. (I) A calibration curve was generated to predict overall survival at 1, 3, and 5 years. (J) Evaluation of risk scores accuracy via DCA curves. ROC, receiver operating characteristic; K-M, Kaplan-Meier; DCA, decision curve analysis.
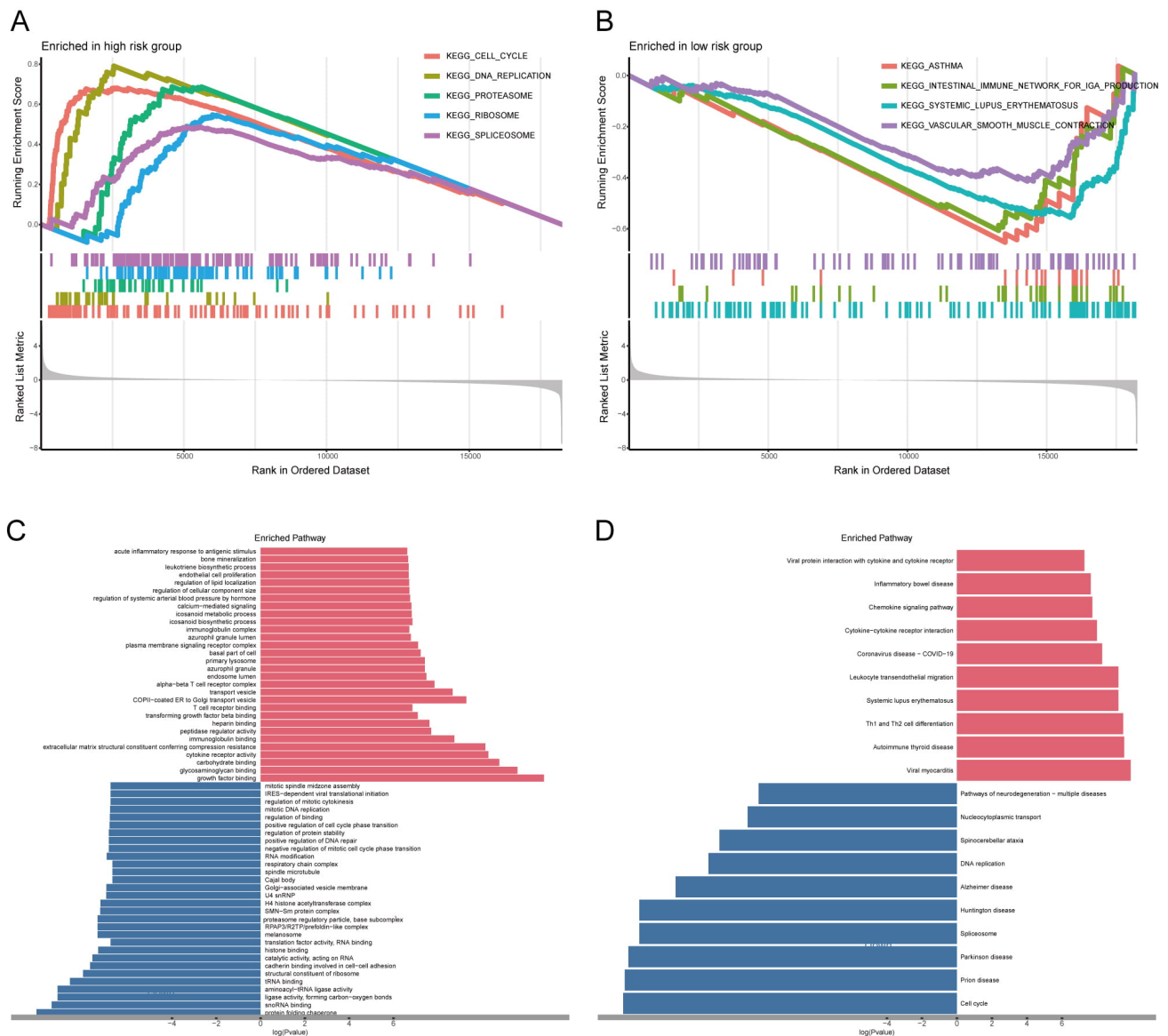
Fig. 7. Enrichment analysis of DEGs across two risk cohorts. (A,B) The GSEA analysis of DEGs between the high- (A) and low-risk cohorts (B). (C,D) GO (C) and KEGG (D) analyses; red color represents the pathway enrichment analysis for genes that are upregulated, whereas blue denotes the pathway enrichment analysis for downregulated genes. GSEA, gene set enrichment analysis.

3.9 Knockdown of SOD3 Inhibits the Growth of Osimertinib-resistant LUAD

We evaluated mRNA expression of the six candidate genes in osimertinib-resistant and parental cell lines. All six genes showed significantly higher mRNA levels in resistant cells than in parental controls ($p < 0.05$; Fig. 11A). Then, we selected SOD3 for further validation due to its central role in redox signaling and strong overexpression in both resistant cells ($p < 0.01$; Fig. 11B). To functionally assess SOD3, we knocked down its expression using shRNA in in HCC827/OR and 1975/OR cells (Fig. 11C,D). SOD3 knockdown significantly restored osimertinib sensitivity ($p < 0.01$; Fig. 11E) and elevated drug-induced ROS accumulation and apoptosis rate (Fig. 11F,G, **Supplementary Fig. 6A,B**). Clinically, SOD3 expression was signif-

icantly lower in third-generation EGFR-TKIs-sensitive patients than in resistant cohorts (Fig. 11H), supporting its role in mediating osimertinib resistance. These results suggest that targeting SOD3 may overcome acquired resistance in LUAD.

4. Discussion

Osimertinib, a third-generation EGFR-TKI, serves as the first-line treatment for EGFR-mutant LUAD. However, acquired resistance remains the primary cause of treatment failure [23,24]. Early detection and effective counterstrategies are crucial to improve patient outcomes. Thus, identifying novel biomarkers that predict prognosis and therapeutic benefits in osimertinib-treated LUAD patients is critically needed.
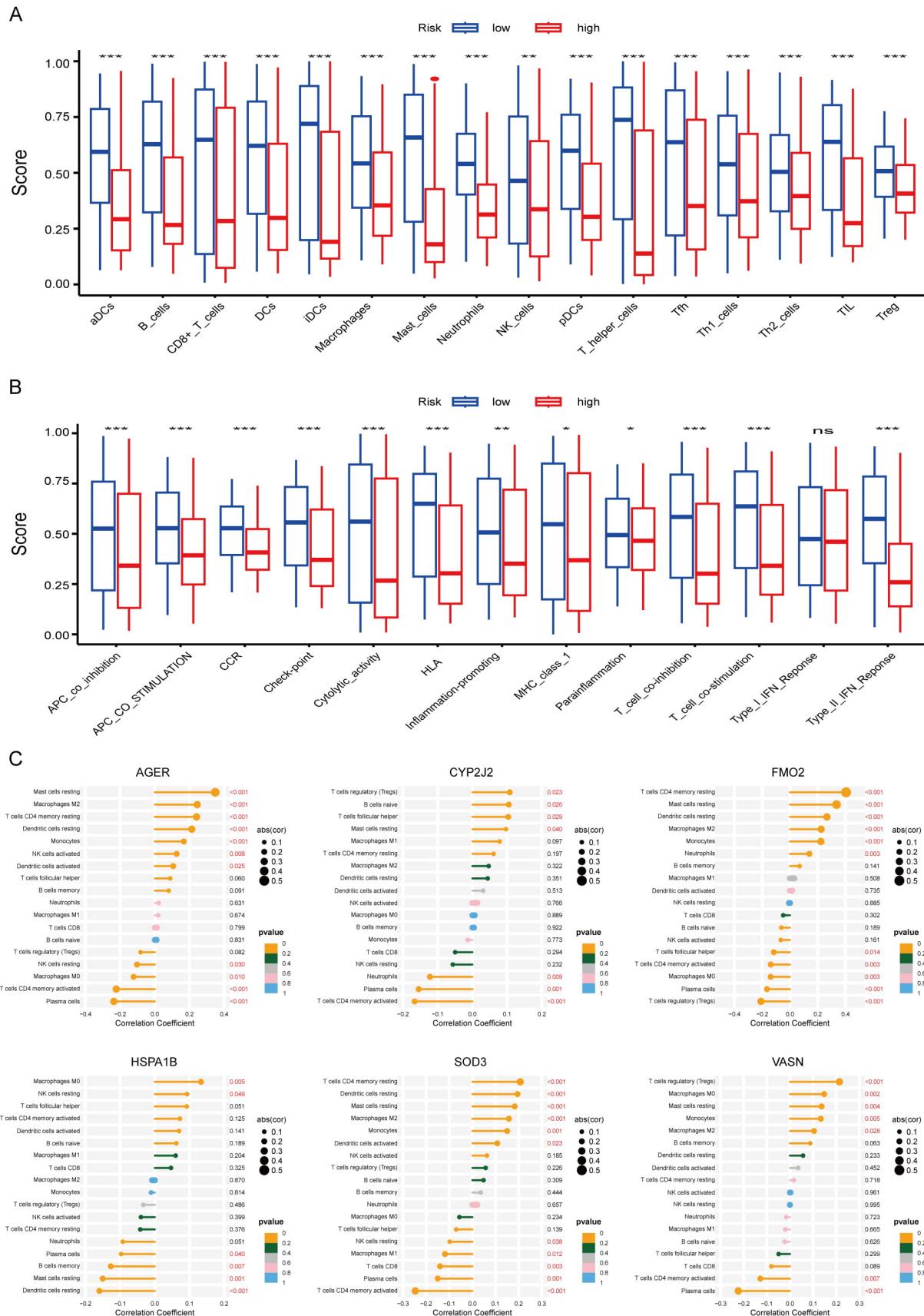
Fig. 8. Analysis of immune microenvironment in LUAD. (A,B) Differences in immune infiltration between the high- and low-risk cohorts; *$p < 0.05$, ** $p < 0.01$, *** $p < 0.001$, ns, not significant. (C) Correlation analysis between the 6 prognostic DE-RRGs and immune cells.
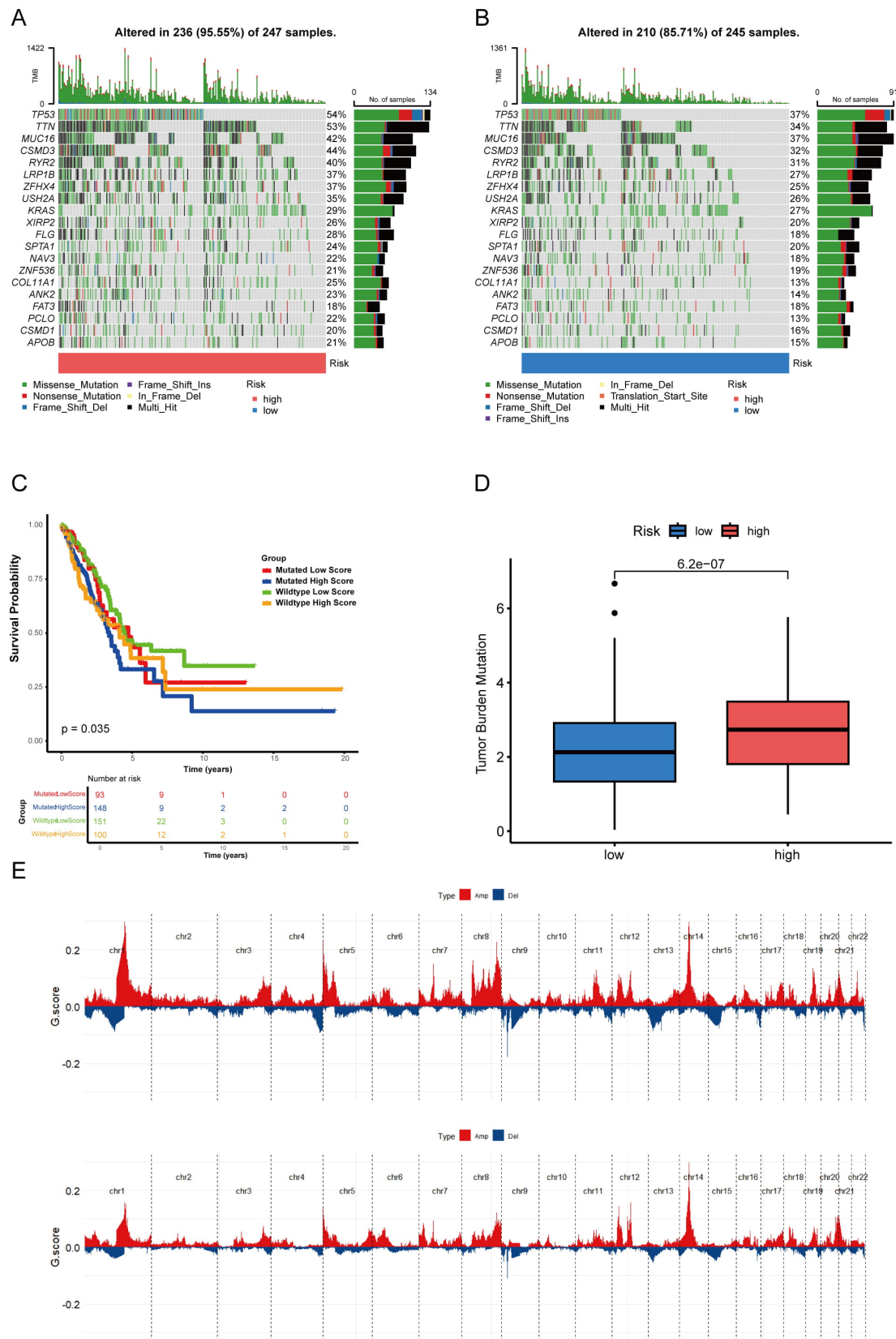
Fig. 9. Analysis of gene mutations in LUAD. (A,B) A waterfall chart displaying somatic mutations in both the two risk cohorts. (C) K–M curves for TCGA-LUAD patients based on the integration of risk scores and *TP53* mutation. (D) Comparison of the TMB between groups categorized into two risk groups. (E) Analysis of copy number variations in two distinct risk groups; amplification mutations are indicated by red lines, whereas blue lines denote deletion mutations.
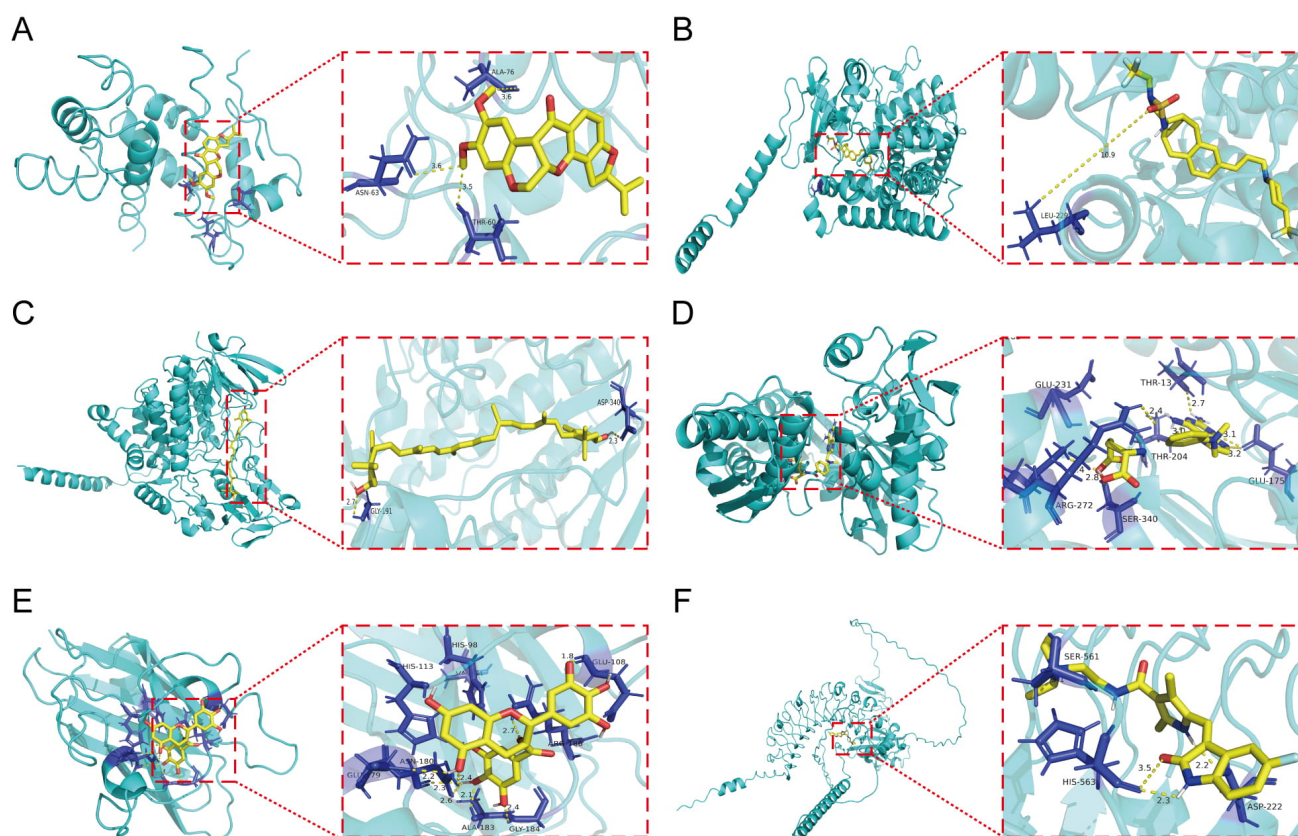
Fig. 10. Small-molecule docking to prognostic DE-RRGs. (A) Docking analysis of AGER in conjunction with rotenone. (B) Docking analysis of CYP2J2 in conjunction with MRK003. (C) Docking analysis of FMO2 in conjunction with lutein. (D) Docking analysis of the interaction of HSPA1B. (E) Docking analysis of SOD3 in conjunction with epigallocatechin gallate. (F) Docking analysis of VASN in conjunction with sunitiib.

Oxidative stress, driven by ROS generation, promotes cancer progression and treatment resistance by disrupting genomic stability and altering signaling pathways [25,26]. Moderate ROS levels can activate key oncogenic pathways, such as nuclear factor kappa-B (NF-κB), phosphatidylinositol 3 kinase (PI3K)/AKT, and p53, while high ROS levels sensitize tumor cells to oxidative death. Many conventional and targeted therapies exert their effects by elevating intracellular ROS. However, cancer cells counteract this through robust antioxidant systems like nuclear factor erythroid-derived 2-like 2/kelch-like ECH-associated protein 1 (NRF2/KEAP1) and B cell lymphoma 2 (BCL2), which enhance survival and confer treatment resistance [27,28]. Targeting oxidative stress has thus become a major therapeutic goal. Notably, redox dysregulation persisted even in models with canonical resistance mechanisms like EGFR-T790M, suggesting that RRG-mediated resistance may complement known pathways [29]. This persistence creates synergistic targeting opportunities, particularly through combining osimertinib with RRG inhibitors alongside MET or EGFR inhibitors, irrespective of the primary resistance mechanism. Tumor heterogeneity further underscores the need to map resistance mechanisms comprehensively. Single-cell RNA sequencing provides a powerful tool to dissect LUAD heterogeneity [30], uncover how redox balance shapes EGFR-TKIs resistance, and identify novel biomarkers.

We analyzed scRNA-seq data from matched OS- and OR-PDX models. The OR group exhibited a higher abundance of CAFs, corroborating prior reports [30]. Cell communication analysis revealed a remodeled interaction network in resistant tumors, with strengthened contacts among Tregs, epithelial cells, CAFs, and tumor cells, notably via the peptidylprolyl isomerase A-basigin (PPIA-BSG) axis, which Liu *et al*. [31] implicated in lung cancer metastasis. CAFs displayed especially enhanced crosstalk with multiple cell types in OR samples. Key hyperactivated ligand-receptor pairs included midkine-syndecan 1 (MDK-SDC1), known to induce immunosuppressive macrophages [32,33], and WNT7B-(FZD2 + LRP5), which promotes tumor progression [34].

We also identified 10 DE-RRGs and assigned RRG activity scores to individual cells. High-scoring cells localized predominantly to CAF clusters, consistent with established roles of CAFs in driving osimertinib resistance through secreted factors like IL-6, periostin, hepatocyte
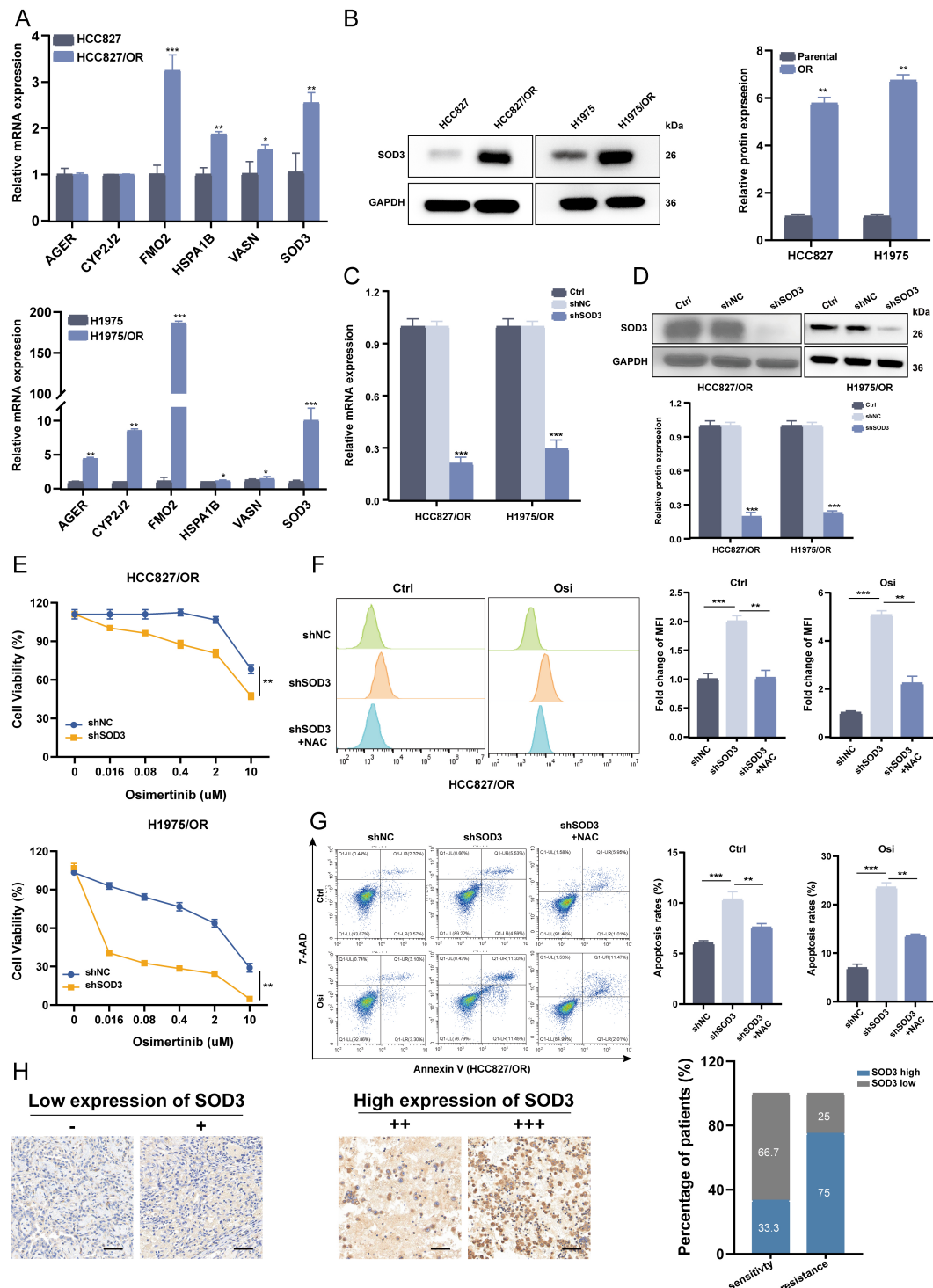
Fig. 11. Knockdown of SOD3 restored osimertinib sensitivity *in vitro*. (A) RT-qPCR was used to assess the mRNA expression of the 6 DE-RRGs in HCC827/OR, H1975/OR and their parental cells. (B) Immunoblot analysis of SOD3 proteins was performed on HCC827/OR cells and their parental counterparts, with representative images obtained from three independent experiments. (C,D) HCC827/OR and H1975/OR cells were transfected with SOD3 shRNA or shNC, and the expression of SOD3 was measured by RT-qPCR (C) and western blotting (D). (E) The viability of HCC827/OR and H1975/OR cells treated with osimertinib was determined by CCK-8 assay after SOD3 knockdown. Data are shown as the mean $\pm$ SEM of three independent experiments. (F,G) HCC827/OR cells underwent or not Osi treatment, then followed by DCFH-DA (F) and were collected for Annexin-V/PI flow cytometry assays (G). (H) Representative IHC images of SOD3 staining in tissues of EGFR-mutant LUAD. (left) SOD3^{low} (-/+), (middle) SOD3^{high} (++/+++), Scale bar = 20 μm; Percentage histogram correlating SOD3 levels with third EGFR-TKIs therapeutic response (EGFR-mutant LUAD cohort); $*p < 0.05$, $**p < 0.01$, $***p < 0.001$.

growth factor (HGF), and insulin-like growth factors (IGFs) [35–38]. Given substantial CAF heterogeneity—including inflammatory CAFs (iCAFs) that recruit immune cells via Eotaxin-1 (CCL11)/Chemokine (C-X-C Motif) Ligand 12 (CXCL12) and matrix-producing CAFs (mCAFs) that over-express ECM-remodeling genes (like matrix metallopro-teinase 11 (MMP11) and collagen type I alpha 1 (COL1A1)) [39]—we classified CAFs into six distinct subtypes. Pseu-dotime analysis indicated that panCAFs arise early and may differentiate into other CAF subtypes, paralleling find-ings in cholangiocarcinoma [40]. During this process, *ABCA1*, *FMO2*, and *KLF2* were downregulated, while *CYP2J2*, *SOD3*, and *VASN* were upregulated, suggesting these RRGs help regulate CAF differentiation. We pro-pose that these DE-RRGs operate during early CAF differ-entiation to enhance intercellular communication, thereby fostering metastasis, resistance, and disease progression. CAFs, as central components of the mesenchymal tumor microenvironment, may thus supply biomarkers, such as specific RRGs or their products, for predicting osimertinib resistance. Further studies should clarify the functional mechanisms of specific CAF subpopulations and RRGs in acquired resistance.

Using parallel scRNA-seq and bulk transcriptome data, we constructed a robust prognostic model based on six DE-RRGs. This model effectively stratified LUAD patients into distinct survival groups. Differential path-way activation revealed potential mechanisms underlying these survival disparities. High-risk scores associated with an immunosuppressive, tumor-progressive microenviron-ment, whereas low-risk scores indicated a more tumor-suppressive milieu. Incorporating TMB further improved prognostic accuracy. Mutation profiles also differed signif-icantly between risk groups, suggesting these patterns could help guide personalized therapeutic strategies for LUAD patients.

Our findings reveal that these genes above are signif-icantly up-regulated to varying degrees in LUAD-OR cell lines, indicating possible role in acquired EGFR-TKIs re-sistance. AGER binds toll-like receptor 4 (TLR4) and me-diates AGE-RAGE signaling, contributing to diabetic an-giopathy and thymic hyperplasia. Previous studies indicate that AGER overexpression suppresses proliferation, inva-sion, and migration in H1299 cells, suggesting a protec-tive role in LUAD with significant prognostic value [41]. However, we found *AGER* positively correlates with M2 macrophage infiltration ($p < 0.001$), a key driver of im-munosuppressive TME. High *AGER* expression in LUAD-OR cells further suggests it might promote osimertinib re-sistance through cell crosstalk. CYP2J2 could epoxidize arachidonic acid into oncogenic epoxyeicosatrienoic acids (EETs). Kojima *et al.* [42] demonstrated that several TKIs suppress NSCLC growth and proliferation by inhibit-ing CYP2J2 activity. Consequently, the observed upreg-ulation of *CYP2J2* in OR cells may represent a compen-

satory mechanism driving therapeutic resistance. FMO2, a flavin-containing monooxygenase (FMO), acts as both a tu-mor suppressor that reduces paclitaxel resistance in LUAD [43] and a tumor promoter that facilitates macrophage infiltration in ovarian cancer [44]. *FMO2* significantly correlated with M2 macrophage infiltration in our study, suggesting it might promotes osimertinib resistance in LUAD via immunosuppression. This reveals a paradoxical pro-tumor role contrasting its known protective functions. HSPA1B encodes HSP70 chaperones that maintain pro-teostasis through protein folding. These proteins promote tumor progression and poor outcomes in cancers including lung cancer. Notably, HSPA1B activation degrades EGFR, potentially delaying TKIs resistance [45,46]. Paradoxi-cally, LUAD-OR cells showed elevated *HSPA1B* mRNA versus parental lines, indicating HSPA1B may drive os-imertinib resistance through EGFR-independent pathways like PI3K-mediated inflammatory upregulation. VASN, primarily expressed in vascular smooth muscle cells, crit-ically regulates neointimal formation post-vascular injury. Its soluble form promotes tumorigenesis by inhibiting trans-forming growth factor-beta (TGF-β) signaling, modulat-ing epithelial-mesenchymal transition, and enhancing an-giogenesis. Functioning as an oncogene, VASN drives can-cer cell proliferation and invasion in multiple malignancies including colorectal cancer and LUAD [47,48]. We ob-served *VASN* overexpression in OR versus parental cells, indicating its potential significance role in EGFR-TKI resis-tance. Unlike other superoxide dismutase (SOD) isoforms, SOD3 localizes primarily to vascular smooth muscle cells and fibroblasts, with peak expression in lungs and blood vessels [49]. Studies have shown that demonstrated that el-evated SOD3 levels in cancer cells confer resistance to di-verse therapeutic strategies, such as chemotherapy, thereby promoting disease progression and correlating with poorer prognosis in NSCLC patients [49,50]. Consistently, we noted increased SOD3 in OR cell models and NSCLC pa-tients with third-generation EGFR-TKI resistance. Meng *et al.* [51] showed ROS accumulation reverses osimertinib resistance in NSCLC by inducing apoptosis. Our findings confirm this mechanism that SOD3 suppression overcomes resistance through ROS accumulation, consistent with its ROS-scavenging function. Understanding the functions of these prognostic genes and the factors that contribute to their negative prognostic significance will be instrumental in formulating combination therapies designed to overcome osimertinib resistance in NSCLC patients.

Drug repurposing represents an innovative therapeu-tic strategy enabled by deepening mechanistic insights into disease pathogenesis. Exemplified by compounds like EGCG, originally anti-inflammatory now investigated in oncology, this paradigm informed our targeted screening of prognostic genes to overcome osimertinib resistance and improve LUAD outcomes. Rotenone binds AGER to downregulate its expression while inhibiting mitochon-

drial complex I, activating NADPH-Oxidase 2 (NOX2)-mediated ROS generation that induces apoptosis in lung cancer cells [52]. This oxidative phosphorylation (OX-PHOS) disruption may counter osimertinib adaptive resistance in NSCLC [53], though mechanisms require further elucidation. MRK003, a potent γ-secretase inhibitor, significantly reduced CYP2J2 expression while inhibiting Notch signaling through suppression of Notch intracellular domain generation. This Notch pathway blockade compromised tumor stemness by impairing self-renewal capacity, chemoresistance, invasive/migratory potential, and *in vivo* tumorigenicity [54]. Consequently, Notch inhibition via MRK003 represents a promising therapeutic strategy to improve survival in LUAD patients [55]. Lutein, a prominent xanthophyll carotenoid found in pigmented fruits, such as kale and spinach [56], demonstrated high-affinity docking with FMO2. Epidemiologically, lutein-rich diets correlate with reduced breast and gastric cancer incidence [57,58]. Mechanistically, lutein suppresses NSCLC tumors by inducing DNA damage and activating the ATR/Chk1/p53 pathway [59]. MTX demonstrated strong binding affinity among compounds screened for HSPA1B mRNA suppression. This dihydrofolate reductase inhibitor depletes tetrahydrofolate pools essential for DNA synthesis and cellular replication [60]. Clinically, concomitant intrathecal MTX and oral afatinib (second-generation TKI) induced more than 10-month clinical remission in an osimertinib-resistant NSCLC patient [61]. Sunitinib demonstrated high-affinity binding to VASN in docking studies, effectively downregulating its expression. As a multi-targeted TKI inhibiting VEGFR and PDGFR, sunitinib exerts broad cytotoxic and anti-angiogenic effects across malignancies through receptor-specific mechanisms. Critically, it exhibits significant synergism with docetaxel against EGFR TKI-resistant NSCLC variants like T790M mutation [62], though further evidence is required to validate its osimertinib-enhancing potential. Our study demonstrated that the natural compound EGCG has a strong affinity for binding to SOD3. As the main biologically active component of green tea, EGCG is part of the polyphenol group and is well-known for its cancer-fighting properties, anti-inflammatory effects, and antioxidant capabilities. EGCG influences glucose metabolism and suppresses the AMPK/AKT/MAPK signaling pathway, which contributes to decreased resistance to osimertinib in NSCLC [63,64]. However, these compounds might exist significant toxicities, such as rotenone causes mitochondrial dysfunction, sunitinib induces cardiovascular side effects, MRK003 promotes tumor neoangiogenesis, and MTX impairs hepatic/renal function. These may severely impair patient quality of life. Therefore, preclinical assessment remains essential to prevent treatment failure or adverse effects during repurposing [52,54,61,62]. Although mechanisms underlying small-molecule enhancement of osimertinib efficacy remain unclear, acquired resistance to EGFR-TKIs persists as a major clinical challenge in EGFR-mutant NSCLC. Our current docking results provide a theoretical basis for the prioritization of compounds. To address this, we propose combining osimertinib with targeted small-molecule inhibitors as promising therapeutics for resistant NSCLC.

We integrated single-cell RNA sequencing to identify osimertinib resistance mechanisms at a subpopulation level, overcoming the resolution limitations of bulk-tissue analysis. To our knowledge, this study establishes the first gene signature specifically predictive of osimertinib resistance in NSCLC, distinct from previous cuproptosis-related prognostic models [65]. Furthermore, we provide novel functional insights into the therapeutic potential of SOD3—a key signature gene—through combined molecular docking and experimental validation, moving beyond purely predictive correlations. However, several limitations should be noted. First, although we show that CAF–tumor cell interactions promote osimertinib resistance, CAF heterogeneity necessitates further subtype-specific investigation using spatial transcriptomics at tumor–CAF niches and co-culture systems with purified CAF subsets. Second, while transcriptomic and functional data suggest metabolic adaptation contributes to resistance, direct validation through metabolic flux assays or lipidomics is needed to quantify changes in ATP generation, glycolysis, and lipid metabolism. Current single-cell datasets remain constrained by limited sample sizes and follow-up data due to high costs. Integrating bulk and single-cell RNA-seq data with advanced computational algorithms will help overcome these constraints. Although RRGs inhibition restored osimertinib sensitivity *in vitro*, future studies should include *in vivo* validation using shRNAs and osimertinib co-treatment in PDX models. Finally, although we identified RRGs mediating resistance, common genomic alterations in LUAD like TP53 mutations may influence redox signaling. Future work should stratify patients by mutation status to refine prognostic biomarkers, prospectively validate the signature's clinical utility and investigate underlying molecular mechanisms.

5. Conclusion

Integrating single-cell and bulk transcriptome analyses, we identified key DE-RRGs as prognostic biomarkers and potential therapeutic targets in LUAD. Our results establish a critical link between redox homeostasis, osimertinib-resistant cell population, and patient survival outcomes. These findings provide novel mechanistic and therapeutic insights for treating lung adenocarcinoma.

Abbreviations

LUAD, lung adenocarcinoma; TME, tumor microenvironment; OR, osimertinib resistance; RRGs, redox-related genes; CAFs, Cancer-associated fibroblasts; NSCLC, non-small cell lung cancer; EGFR, epidermal

growth factor receptor; TKIs, tyrosine kinase inhibitors; ROS, reactive oxygen species; scRNA-seq, single-cell RNA sequencing; DE-RRGs, differentially expressed redox-related genes; PDX, patient-derived xenograft; TCGA, cancer genome atlas; GEO, gene expression omnibus; t-SNE, t-distributed stochastic neighbor embedding; LASSO, least absolute shrinkage and selection operator; ROC, receiver operating characteristic; GO, gene ontology; KEGG, kyoto encyclopedia of Genes and Genomes; ssGSEA, single-sample gene set enrichment analysis; TMB, tumor mutational burden; CNVs, copy number variations; IHC, immunohistochemistry; DEGs, differentially expressed genes; OS, osimertinib sensitivity; MTX, methotrexate; EGCG, epigallocatechin gallate; TLR4, toll-like receptor 4; AGER, advanced glycosylation end product-specific receptor; CYP2J2, cytochrome P450 family 2 subfamily J polypeptide 2; HSPA1B, heat shock 70 kDa protein 1B; FMO2, flavin-containing monooxygenase 2; VASN, vasorin; SOD3, superoxide dismutase 3; KLF2, kruppel like factor 2; ABCA1, ATP-binding cassette transporter A1; GSTA4, Glutathione S Transferase A4; AGE-RAGE, advanced glycation end products-receptor for advanced glycation end products; mesCAFs, mesothelial CAF; UMAP, Uniform Manifold Approximation and Projection; NF-κB, nuclear factor kappa-B; PI3K, phosphatidylinositol 3 kinase; NRF2/KEAP1, nuclear factor erythroid-derived 2-like 2/Kelch-like ECH-associated protein 1; BCL2, B cell lymphoma 2; AKT, protein kinase B; FAK, focal adhesion kinase; PPIA-BSG, peptidylprolyl isomerase A-basigin; MDK-SDC1, midkine-syndecan 1; HGF, hepatocyte growth factor; IGFs, insulin-like growth factors; CCL11, Eotaxin-1; CXCL12, Chemokine (C-X-C Motif) Ligand 12; MMP11, matrix metalloproteinase 11; COL1A1, collagen type I alpha 1.

Availability of Data and Materials

The data generated or analysed to support the findings during this study are available from the TCGA (https://portal.gdc.cancer.gov/) and GEO (https://www.ncbi.nlm.nih.gov/geo/) open database. The datasets used and analyzed during the current study are available from the corresponding author on reasonable request.

Author Contributions

FQ designed the study. CF and DL made contribution to the data analyses and drew up the manuscript. CL and RQ finished statistical analysis for the data. GZ, FY and CS conducted molecular experiments. JD and TL processed figures and tables. FQ undertook support for the project. All authors contributed to editorial changes in the manuscript. All authors read and approved the final manuscript. All authors have participated sufficiently in the work and agreed to be accountable for all aspects of the work.

Ethics Approval and Consent to Participate

The information utilized in this research was sourced from publicly available databases. The samples were derived from the pathological specimen bank of the First Affiliated Hospital of Nanchang University [Ethics Approval Number: (2024) CDYFYYLK (10-005)] and abided by the rules of the Declaration of Helsinki. All patients or their guardians signed informed consent forms.

Acknowledgment

Not applicable.

Conflict of Interest

The authors declare no conflict of interest.

Supplementary Material

Supplementary material associated with this article can be found, in the online version, at https://doi.org/10.31083/FBL40454.

References

[1] Siegel RL, Giaquinto AN, Jemal A. Cancer statistics, 2024. CA: a Cancer Journal for Clinicians. 2024; 74: 12–49. https://doi.org/10.3322/caac.21820.

[2] Ramalingam SS, Vansteenkiste J, Planchard D, Cho BC, Gray JE, Ohe Y, *et al*. Overall Survival with Osimertinib in Untreated, *EGFR*-Mutated Advanced NSCLC. The New England Journal of Medicine. 2020; 382: 41–50. https://doi.org/10.1056/NEJMoa1913662.

[3] Shaban N, Kamashev D, Emelianova A, Buzdin A. Targeted Inhibitors of EGFR: Structure, Biology, Biomarkers, and Clinical Applications. Cells. 2023; 13: 47. https://doi.org/10.3390/cells13010047.

[4] Cooper AJ, Sequist LV, Lin JJ. Third-generation EGFR and ALK inhibitors: mechanisms of resistance and management. Nature Reviews. Clinical Oncology. 2022; 19: 499–514. https://doi.org/10.1038/s41571-022-00639-9.

[5] Fu K, Xie F, Wang F, Fu L. Therapeutic strategies for EGFR-mutated non-small cell lung cancer patients with osimertinib resistance. Journal of Hematology & Oncology. 2022; 15: 173. https://doi.org/10.1186/s13045-022-01391-4.

[6] Lennicke C, Cochemé HM. Redox metabolism: ROS as specific molecular regulators of cell signaling and function. Molecular Cell. 2021; 81: 3691–3707. https://doi.org/10.1016/j.molcel.2021.08.018.

[7] DeNicola GM, Karreth FA, Humpton TJ, Gopinathan A, Wei C, Frese K, *et al*. Oncogene-induced Nrf2 transcription promotes ROS detoxification and tumorigenesis. Nature. 2011; 475: 106–109. https://doi.org/10.1038/nature10189.

[8] Rojo de la Vega M, Chapman E, Zhang DD. NRF2 and the Hallmarks of Cancer. Cancer Cell. 2018; 34: 21–43. https://doi.org/10.1016/j.ccell.2018.03.022.

[9] Iqbal MJ, Kabeer A, Abbas Z, Siddiqui HA, Calina D, Sharifi-Rad J, et al. Interplay of oxidative stress, cellular communication and signaling pathways in cancer. Cell Communication and Signaling: CCS. 2024; 22: 7. https://doi.org/10.1186/s12964-023-01398-5.

[10] Zhou C, Yu T, Zhu R, Lu J, Ouyang X, Zhang Z, et al. Timosaponin AIII promotes non-small-cell lung cancer ferroptosis through targeting and facilitating HSP90 mediated GPX4 ubiquitination and degradation. International Journal of Biological Sciences. 2023; 19: 1471–1489. https://doi.org/10.7150/ijbs.77979.

[11] Bluemel G, Planque M, Madreiter-Sokolowski CT, Haitzmann T, Hrzenjak A, Graier WF, et al. PCK2 opposes mitochondrial respiration and maintains the redox balance in starved lung cancer cells. Free Radical Biology & Medicine. 2021; 176: 34–45. https://doi.org/10.1016/j.freeradbiomed.2021.09.007.

[12] Lan T, Arastu S, Lam J, Kim H, Wang W, Wang S, et al. Glucose-6-phosphate dehydrogenase maintains redox homeostasis and biosynthesis in LKB1-deficient KRAS-driven lung cancer. Nature Communications. 2024; 15: 5857. https://doi.org/10.1038/s41467-024-50157-8.

[13] Zhang D, Hou Z, Aldrich KE, Lockwood L, Odom AL, Liby KT. A Novel Nrf2 Pathway Inhibitor Sensitizes Keap1-Mutant Lung Cancer Cells to Chemotherapy. Molecular Cancer Therapeutics. 2021; 20: 1692–1701. https://doi.org/10.1158/1535-7163.MCT-21-0210.

[14] Bischoff P, Trinks A, Obermayer B, Pett JP, Wiederspahn J, Uhlitz F, et al. Single-cell RNA sequencing reveals distinct tumor microenvironmental patterns in lung adenocarcinoma. Oncogene. 2021; 40: 6748–6758. https://doi.org/10.1038/s41388-021-02054-3.

[15] Wang L, Liu Y, Dai Y, Tang X, Yin T, Wang C, et al. Single-cell RNA-seq analysis reveals BHLHE40-driven pro-tumour neutrophils with hyperactivated glycolysis in pancreatic tumour microenvironment. Gut. 2023; 72: 958–971. https://doi.org/10.1136/gutjnl-2021-326070.

[16] Lei H, Guo XA, Tao Y, Ding K, Fu X, Oesterreich S, et al. Semi-deconvolution of bulk and single-cell RNA-seq data with application to metastatic progression in breast cancer. Bioinformatics (Oxford, England). 2022; 38: i386–i394. https://doi.org/10.1093/bioinformatics/btac262.

[17] Wang Z, Chen C, Ai J, Shu J, Ding Y, Wang W, et al. Identifying mitophagy-related genes as prognostic biomarkers and therapeutic targets of gastric carcinoma by integrated analysis of single-cell and bulk-RNA sequencing data. Computers in Biology and Medicine. 2023; 163: 107227. https://doi.org/10.1016/j.compbiomed.2023.107227.

[18] Zheng M, Hu Y, Liu O, Li S, Wang Y, Li X, et al. Oxidative Stress Response Biomarkers of Ovarian Cancer Based on Single-Cell and Bulk RNA Sequencing. Oxidative Medicine and Cellular Longevity. 2023; 2023: 1261039. https://doi.org/10.1155/2023/1261039.

[19] Yang C, Zhang J, Xie J, Li L, Zhao X, Liu J, et al. Identification of Cancer Stem Cell-related Gene by Single-cell and Machine Learning Predicts Immune Status, Chemotherapy Drug, and Prognosis in Lung Adenocarcinoma. Current Stem Cell Research & Therapy. 2024; 19: 767–780. https://doi.org/10.2174/1574888X18666230714151746.

[20] Zhang J, Liu X, Huang Z, Wu C, Zhang F, Han A, et al. T cell-related prognostic risk model and tumor immune environment modulation in lung adenocarcinoma based on single-cell and bulk RNA sequencing. Computers in Biology and Medicine. 2023; 152: 106460. https://doi.org/10.1016/j.compbiomed.2022.106460.

[21] Du Z, Zhang T, Lin Y, Dong G, Li A, Wang Z, et al. A prognostic model of drug tolerant persister-related genes in lung adenocarcinoma based on single cell and bulk RNA sequencing data. Heliyon. 2023; 9: e20708. https://doi.org/10.1016/j.heliyon.2023.e20708.

[22] Lai J, Fang C, Zhang G, Shi C, Yu F, Gu W, et al. Novel Prognostic Model Construction of Tongue Squamous Cell Carcinoma Based on Apigenin-Associated Genes. Frontiers in Bioscience (Landmark Edition). 2024; 29: 65. https://doi.org/10.31083/j.fbl2902065.

[23] Herbst RS, Wu YL, John T, Grohe C, Majem M, Wang J, et al. Adjuvant Osimertinib for Resected EGFR-Mutated Stage IB-IIIA Non-Small-Cell Lung Cancer: Updated Results From the Phase III Randomized ADAURA Trial. Journal of Clinical Oncology: Official Journal of the American Society of Clinical Oncology. 2023; 41: 1830–1840. https://doi.org/10.1200/JCO.22.02186.

[24] Remon J, Besse B, Aix SP, Callejo A, Al-Rabi K, Bernabe R, et al. Osimertinib treatment based on plasma T790M monitoring in patients with EGFR-mutant non-small-cell lung cancer (NSCLC): EORTC Lung Cancer Group 1613 APPLE phase II randomized clinical trial. Annals of Oncology: Official Journal of the European Society for Medical Oncology. 2023; 34: 468–476. https://doi.org/10.1016/j.annonc.2023.02.012.

[25] Zhang KR, Zhang YF, Lei HM, Tang YB, Ma CS, Lv QM, et al. Targeting AKR1B1 inhibits glutathione de novo synthesis to overcome acquired resistance to EGFR-targeted therapy in lung cancer. Science Translational Medicine. 2021; 13: eabg6428. https://doi.org/10.1126/scitranslmed.abg6428.

[26] Bhasin N, Dabral P, Senavirathna L, Pan S, Chen R. Inhibition of TRAP1 Accelerates the DNA Damage Response, Activation of the Heat Shock Response and Metabolic Reprogramming in Colon Cancer Cells. Frontiers in bioscience (Landmark edition). 2023; 28: 227. https://doi.org/10.31083/j.fbl2809227.

[27] Lin W, Wang X, Diao M, Wang Y, Zhao R, Chen J, et al. Promoting reactive oxygen species accumulation to overcome tyrosine kinase inhibitor resistance in cancer. Cancer Cell International. 2024; 24: 239. https://doi.org/10.1186/s12935-024-03418-x.

[28] Zhang Z, Tan Y, Huang C, Wei X. Redox signaling in drug-tolerant persister cells as an emerging therapeutic target. EBioMedicine. 2023; 89: 104483. https://doi.org/10.1016/j.ebiom.2023.104483.

[29] Peng H, Chen B, Huang W, Tang Y, Jiang Y, Zhang W, et al. Reprogramming Tumor-Associated Macrophages To Reverse EGFR^{T790M} Resistance by Dual-Targeting Codelivery of Gefitinib/Vorinostat. Nano Letters. 2017; 17: 7684–7690. https://doi.org/10.1021/acs.nanolett.7b03756.

[30] Huang Y, Wang X, Wen C, Wang J, Zhou H, Wu L. Cancer-associated fibroblast-derived colony-stimulating factor 2 confers acquired osimertinib resistance in lung adenocarcinoma via promoting ribosome biosynthesis. MedComm. 2024; 5: e653. https://doi.org/10.1002/mco2.653.

[31] Liu L, Zhou Y, Ye Z, Chen Z, Yuan B, Guo L, et al. Single-cell profiling uncovers the intricate pathological niche diversity in brain, lymph node, bone, and adrenal metastases of lung cancer. Discover Oncology. 2025; 16: 512. https://doi.org/10.1007/s12672-025-02269-w.

[32] Hu XF, Yao J, Gao SG, Yang YT, Peng XQ, Feng XS. Midkine and syndecan 1 levels correlate with the progression of malignant gastric cardiac adenocarcinoma. Molecular Medicine Reports. 2014; 10: 1409–1415. https://doi.org/10.3892/mmr.2014.2369.

[33] Zhang Y, Zuo C, Liu L, Hu Y, Yang B, Qiu S, et al. Single-cell RNA-sequencing atlas reveals an MDK-dependent immunosuppressive environment in ErbB pathway-mutated gallbladder can-

cer. Journal of Hepatology. 2021; 75: 1128–1141. https://doi.org/10.1016/j.jhep.2021.06.023.

[34] Yuzugullu H, Benhaj K, Ozturk N, Senturk S, Celik E, Toylu A, *et al*. Canonical Wnt signaling is antagonized by noncanonical Wnt5a in hepatocellular carcinoma cells. Molecular Cancer. 2009; 8: 90. https://doi.org/10.1186/1476-4598-8-90.

[35] Ochi K, Suzawa K, Thu YM, Takatsu F, Tsudaka S, Zhu Y, *et al*. Drug repositioning of tranilast to sensitize a cancer therapy by targeting cancer-associated fibroblast. Cancer Science. 2022; 113: 3428–3436. https://doi.org/10.1111/cas.15502.

[36] Remsing Rix LL, Sumi NJ, Hu Q, Desai B, Bryant AT, Li X, *et al*. IGF-binding proteins secreted by cancer-associated fibroblasts induce context-dependent drug sensitization of lung cancer cells. Science Signaling. 2022; 15: eabj5879. https://doi.org/10.1126/scisignal.abj5879.

[37] Takatsu F, Suzawa K, Tomida S, Thu YM, Sakaguchi M, Toji T, *et al*. Periostin secreted by cancer-associated fibroblasts promotes cancer progression and drug resistance in non-small cell lung cancer. Journal of Molecular Medicine (Berlin, Germany). 2023; 101: 1603–1614. https://doi.org/10.1007/s00109-023-02384-7.

[38] Zhu K, Lv Z, Xiong J, Zheng H, Zhang S, Jin H, *et al*. MET inhibitor, capmatinib overcomes osimertinib resistance via suppression of MET/Akt/snail signaling in non-small cell lung cancer and decreased generation of cancer-associated fibroblasts. Aging. 2021; 13: 6890–6903. https://doi.org/10.18632/aging.202547.

[39] Ma C, Yang C, Peng A, Sun T, Ji X, Mi J, *et al*. Pan-cancer spatially resolved single-cell analysis reveals the crosstalk between cancer-associated fibroblasts and tumor microenvironment. Molecular Cancer. 2023; 22: 170. https://doi.org/10.1186/s12943-023-01876-x.

[40] Zhang M, Yang H, Wan L, Wang Z, Wang H, Ge C, *et al*. Single-cell transcriptomic architecture and intercellular crosstalk of human intrahepatic cholangiocarcinoma. Journal of Hepatology. 2020; 73: 1118–1130. https://doi.org/10.1016/j.jhep.2020.05.039.

[41] Wang Q, Zhu W, Xiao G, Ding M, Chang J, Liao H. Effect of AGER on the biological behavior of non small cell lung cancer H1299 cells. Molecular Medicine Reports. 2020; 22: 810–818. https://doi.org/10.3892/mmr.2020.11176.

[42] Kojima A, Nadai M, Murayama N, Yamazaki H, Katoh M. Effects of tyrosine kinase inhibitors used for the treatment of non-small cell lung carcinoma on cytochrome P450 2J2 activities. Xenobiotica; the Fate of Foreign Compounds in Biological Systems. 2024; 54: 642–647. https://doi.org/10.1080/00498254.2024.2389401.

[43] Qian X, Chen C, Tong S, Zhang J. Circ_MACF1 targets miR-421 to upregulate FMO2 to suppress paclitaxel resistance and malignant cellular behaviors in lung adenocarcinoma. Thoracic Cancer. 2023; 14: 3348–3357. https://doi.org/10.1111/1759-7714.15132.

[44] Yu S, Yang R, Xu T, Li X, Wu S, Zhang J. Cancer-associated fibroblasts-derived FMO2 as a biomarker of macrophage infiltration and prognosis in epithelial ovarian cancer. Gynecologic Oncology. 2022; 167: 342–353. https://doi.org/10.1016/j.ygyno.2022.09.003.

[45] Guo H, Deng Q, Wu C, Hu L, Wei S, Xu P, *et al*. Variations in HSPA1B at 6p21.3 are associated with lung cancer risk and prognosis in Chinese populations. Cancer Research. 2011; 71: 7576–7586. https://doi.org/10.1158/0008-5472.CAN-11-1409.

[46] Hong X, Hsieh MT, Tseng TY, Lin HY, Chang HC, Yau ST, *et al*. Diarylheptanoid 35d overcomes EGFR TKI resistance by inducing hsp70-mediated lysosomal degradation of EGFR in EGFR-mutant lung adenocarcinoma. The Journal of Biological Chemistry. 2023; 299: 104814. https://doi.org/10.1016/j.jb

c.2023.104814.

[47] Liang W, Zuo J, Liu M, Su Y, Guo B, Hou J, *et al*. VASN promotes colorectal cancer progression by activating the YAP/TAZ and AKT signaling pathways via YAP. FASEB Journal: Official Publication of the Federation of American Societies for Experimental Biology. 2023; 37: e22688. https://doi.org/10.1096/fj.202201181R.

[48] Wu DN, Zhang KL, Chen RH, Ye WS, Zheng C, Zheng YL, *et al*. VASN promotes the aggressive phenotype in ARID1A-deficient lung adenocarcinoma. BMC Cancer. 2024; 24: 1327. https://doi.org/10.1186/s12885-024-13083-y.

[49] Zhang Y, Lu X, Zhang Y, Zhao D, Gong H, Du Y, *et al*. The Effect of Extracellular Superoxide Dismutase (SOD3) Gene in Lung Cancer. Frontiers in Oncology. 2022; 12: 722646. https://doi.org/10.3389/fonc.2022.722646.

[50] Zelko IN, Mariani TJ, Folz RJ. Superoxide dismutase multigene family: a comparison of the CuZn-SOD (SOD1), Mn-SOD (SOD2), and EC-SOD (SOD3) gene structures, evolution, and expression. Free Radical Biology & Medicine. 2002; 33: 337–349. https://doi.org/10.1016/s0891-5849(02)00905-x.

[51] Meng Y, Lin W, Wang N, Wei X, Mei P, Wang X, *et al*. USP7-mediated ERβ stabilization mitigates ROS accumulation and promotes osimertinib resistance by suppressing PRDX3 SUMOylation in non-small cell lung carcinoma. Cancer Letters. 2024; 582: 216587. https://doi.org/10.1016/j.canlet.2023.216587.

[52] Cruz-Bermúdez A, Laza-Briviesca R, Vicente-Blanco RJ, García-Grande A, Coronado MJ, Laine-Menéndez S, *et al*. Cisplatin resistance involves a metabolic reprogramming through ROS and PGC-1α in NSCLC which can be overcome by OXPHOS inhibition. Free Radical Biology & Medicine. 2019; 135: 167–181. https://doi.org/10.1016/j.freeradbiomed.2019.03.009.

[53] Wang H, Hu Q, Chen Y, Huang X, Feng Y, Shi Y, *et al*. Ferritinophagy mediates adaptive resistance to EGFR tyrosine kinase inhibitors in non-small cell lung cancer. Nature Communications. 2024; 15: 4195. https://doi.org/10.1038/s41467-024-48433-8.

[54] Xiao W, Gao Z, Duan Y, Yuan W, Ke Y. Notch signaling plays a crucial role in cancer stem-like cells maintaining stemness and mediating chemotaxis in renal cell carcinoma. Journal of Experimental & Clinical Cancer Research: CR. 2017; 36: 41. https://doi.org/10.1186/s13046-017-0507-3.

[55] Hassan KA, Wang L, Korkaya H, Chen G, Maillard I, Beer DG, *et al*. Notch pathway activity identifies cells with cancer stem cell-like properties and correlates with worse survival in lung adenocarcinoma. Clinical Cancer Research: an Official Journal of the American Association for Cancer Research. 2013; 19: 1972–1980. https://doi.org/10.1158/1078-0432.CCR-12-0370.

[56] Saini RK, Keum YS, Daglia M, Rengasamy KR. Dietary carotenoids in cancer chemoprevention and chemotherapy: A review of emerging evidence. Pharmacological Research. 2020; 157: 104830. https://doi.org/10.1016/j.phrs.2020.104830.

[57] Eliassen AH, Liao X, Rosner B, Tamimi RM, Tworoger SS, Hankinson SE. Plasma carotenoids and risk of breast cancer over 20 y of follow-up. The American Journal of Clinical Nutrition. 2015; 101: 1197–1205. https://doi.org/10.3945/ajcn.114.105080.

[58] Kim JH, Lee J, Choi IJ, Kim YI, Kwon O, Kim H, *et al*. Dietary Carotenoids Intake and the Risk of Gastric Cancer: A Case-Control Study in Korea. Nutrients. 2018; 10: 1031. https://doi.org/10.3390/nu10081031.

[59] Zhang SY, Lu YY, He XL, Su Y, Hu F, Wei XS, *et al*. Lutein inhibits tumor progression through the ATR/Chk1/p53 signaling pathway in non-small cell lung cancer. Phytotherapy Research: PTR. 2023; 37: 1260–1273. https://doi.org/10.1002/ptr.7682.

[60] Hamed KM, Dighriri IM, Baomar AF, Alharthy BT, Alenazi

FE, Alali GH, *et al*. Overview of Methotrexate Toxicity: A Comprehensive Literature Review. Cureus. 2022; 14: e29518. https://doi.org/10.7759/cureus.29518.

[61] Li G, Fang M, Zhou Y, Liu X, Tian P, Mei F. Afatinib overcoming resistance to icotinib and osimertinib in NSCLC with leptomeningeal metastasis in patients with acquired EGFR L858R/T790M or L858R/S768I mutations: Two case reports. Heliyon. 2023; 9: e20690. https://doi.org/10.1016/j.heliyon.2023.e20690.

[62] Pan F, Tian J, Zhang X, Zhang Y, Pan Y. Synergistic interaction between sunitinib and docetaxel is sequence dependent in human non-small lung cancer with EGFR TKIs-resistant mutation. Journal of Cancer Research and Clinical Oncology. 2011; 137: 1397–1408. https://doi.org/10.1007/s00432-011-1009-x.

[63] Ma YC, Li C, Gao F, Xu Y, Jiang ZB, Liu JX, *et al*. Epigallocatechin gallate inhibits the growth of human lung cancer by directly targeting the EGFR signaling pathway. Oncology Reports. 2014; 31: 1343–1349. https://doi.org/10.3892/or.2013.2933.

[64] Zhou Y, Huang S, Guo Y, Ran M, Shan W, Chen WH, *et al*. Epigallocatechin gallate circumvents drug-induced resistance in non-small-cell lung cancer by modulating glucose metabolism and AMPK/AKT/MAPK axis. Phytotherapy Research: PTR. 2023; 37: 5837–5853. https://doi.org/10.1002/ptr.7990.

[65] Li P, Li J, Wen F, Cao Y, Luo Z, Zuo J, *et al*. A novel cuproptosis-related LncRNA signature: Prognostic and therapeutic value for acute myeloid leukemia. Frontiers in Oncology. 2022; 12: 966920. https://doi.org/10.3389/fonc.2022.966920.